Journal of Computational Physics 404 (2020) 109062

Contents lists available at ScienceDirect

Journal of Computational Physics

www.elsevier.com/locate/jcp

An efficient class of WENO schemes with adaptive order for unstructured meshes

Dinshaw S. Balsara [a,b,*], Sudip Garain [b], Vladimir Florinski [c], Walter Boscheri [d]

[a] ACMS Department, University of Notre Dame, United States of America
[b] Physics Department, University of Notre Dame, United States of America
[c] Space Physics, University of Alabama, Huntsville, United States of America
[d] Department of Mathematics and Computer Science, University of Ferrara, Italy

ARTICLE INFO

Article history:
Received 27 June 2018
Received in revised form 22 October 2019
Accepted 23 October 2019
Available online 6 November 2019

Keywords:
Higher order schemes
Hyperbolic systems
WENO
Reconstruction

ABSTRACT

Recent advances in finite-difference WENO schemes for hyperbolic conservation laws have resulted in WENO schemes with adaptive order of accuracy. For instance, a WENO-AO(5,3) scheme can provide up to fifth order of accuracy when the smoothness of the solution in the fifth order stencil warrants it, and yet, it can adaptively drop down to third order of accuracy when the higher order is not warranted by the solution on the mesh. Having an analogous capability for finite-volume WENO schemes for hyperbolic conservation laws, especially on unstructured meshes, can be very valuable. The present paper documents the design of finite volume WENO-AO(4,3) and WENO-AO(5,3) schemes for unstructured meshes. As with WENO-AO for structured meshes, the key advance lies in realizing that there is a favorable basis set, which is very easily constructed, and in which the computation is dramatically simplified. As with finite-difference WENO, we realize that one can make a non-linear hybridization between a large, centered, very high accuracy stencil and a lower order central WENO scheme that is, nevertheless, very stable and capable of capturing physically meaningful extrema. This yields a class of adaptive order WENO schemes that work well on unstructured meshes. On both the large and small stencils we have been able to make the stencil evaluation step very efficient owing to the choice of a favorable Taylor series basis. By extending the Parallel Axis Theorem, we show that there is a significant simplification in the finite volume reconstruction. Instead of solving a constrained least squares problem, our method only requires the solution of a smaller least squares problem on each stencil. This also simplifies the matrix assembly and solution for each stencil. The evaluation of smoothness indicators is also simplified. Accuracy tests show that the method meets its design accuracy. Several stringent test problems are presented to demonstrate that the method works very robustly and very well. The test problems are chosen to show that our method can be applied to many different meshes that are used to map geometric complexity or solution complexity.

* Corresponding author.
E-mail addresses: dbalsara@nd.edu (D.S. Balsara), sgarain@nd.edu (S. Garain), vaf0001@uah.edu (V. Florinski), walter.boscheri@unife.it (W. Boscheri).

https://doi.org/10.1016/j.jcp.2019.109062
0021-9991/

1. Introduction

Weighted Essentially Non-Oscillatory (WENO) schemes constitute one of the earliest numerical strategies for obtaining the solution to hyperbolic conservation laws with better than second order accuracy in the vicinity of smooth flows. They have also emerged as one of the most popular and well-used methods for delivering high order of accuracy at modest computational cost to the practicing scientist and engineer. The fact that they are well-known, easy to implement and offer good non-linear hybridization at local discontinuities adds to their attractiveness. Even so, very high order WENO schemes have been difficult to implement on unstructured meshes. The goal of this paper is, therefore, to show that there is an easy-to-implement strategy for achieving high order of accuracy on unstructured meshes. The method presented here builds on two recent innovations that have been carried out for finite difference WENO on structured meshes (Balsara, Garain and Shu [14]). The first innovation consists of choosing a suitable expansion basis in which the reconstruction problem on each stencil becomes simpler. The second innovation consists of combining only one large and very high order stencil with several smaller third order stencils (which nevertheless preserve physical extrema). In this paper we show that the same two innovations extend to unstructured meshes. The upshot is that anyone with a third order CWENO-type scheme that has been implemented on unstructured meshes (Semplice et al. [59], Dumbser et al. [36,37], Cravero et al. [31]) should be able to extend their code to higher order of accuracy using the methods described here. In fact, many of the popular WENO approaches for unstructured meshes (for example, Friedrichs [38], Dumbser and Käser [34]) should also find our methods very useful. This extension can be made with minimal effort.

All WENO schemes find their origins in Essentially Non-Oscillatory (ENO) schemes which were formulated in finite volume form by Harten et al. [42] and later in finite difference form by Shu and Osher [60,61]. The method was based on analyzing multiple high order stencils in order to find the single unique one that was most likely to produce a reconstructed polynomial with the smallest variation in the reconstructed solution. The use of a single stencil was found to be numerically unstable since certain types of pathological initial conditions could be designed that yielded too rapid a switching between stencils from one zone to the next. This rapid switching of stencils resulted in a loss of accuracy. Liu, Osher and Chan [51] and Jiang and Shu [47] overcame this problem by designing a fifth order finite-difference Weighted Essentially Non-Oscillatory (WENO) scheme for structured meshes. The same reconstruction strategy was extended up to eleventh order by Balsara and Shu [4] and nineteenth order by Gerolymos, Sénéchal and Vallet [39]; see also Aràndiga et al. [3]. The baseline finite difference WENO scheme has seen many improvements. A formulation of WENO that preserves accuracy at critical points was presented in Henrick, Aslam & Powers [43], Borges et al. [22] and Castro et al. [28]. Balsara et al. [7] and Balsara, Garain and Shu [14] showed that the smoothness indicators for all orders of finite-difference WENO could be written very compactly in terms of the sum of perfect squares. Don et al. [33] have shown the value of the above compactly-written smoothness indicators in preserving symmetry for numerical calculations. The finite volume WENO methods have also been adapted to handle complex geometry by Hu and Shu [44] and Liu and Zhang [54]. The WENO reconstruction philosophy has also shown itself to be very malleable for use in constraint-preserving reconstruction of vector fields, as is needed in magnetohydrodynamics or computational electrodynamics (Balsara [5–8], Balsara and Dumbser [13], Xu, Balsara and Du [70], Balsara et al. [16–18]). For a comprehensive review of WENO schemes, see Shu [62]. To see how WENO schemes fit into the range of available higher order schemes, see the review by Balsara [19]. Several authors, too many to be mentioned, have contributed to the development of WENO schemes. Amongst the other noteworthy contributions we mention (Barth and Frederickson [21], Abgrall [1], Tsoutsanis et al. [67], Zhang and Shu [71], Aboiyar et al. [2]).

The high accuracy that can be achieved by finite difference WENO schemes has shown its use in idealized studies of turbulence. Numerical studies of turbulence require careful attention to accuracy and phase errors (Lele [49], Tam and Webb [66]). Compact-WENO schemes have been designed to handle shocks and simultaneously increase the phase accuracy (Pirozzoli [58], Shen and Yang [63], Deng and Zhang [32], Hu et al. [46], Martin et al. [57], Johnsen et al. [48]). As simulations of turbulence move on to the treatment of complex geometry, the same advantages of high accuracy will be needed on unstructured meshes. One may, therefore, expect that the schemes presented here might be useful for the simulation of turbulent engineering flows in complex geometries.

The original finite-difference WENO schemes (Jiang and Shu [47], Balsara and Shu [14]) achieve their high order of accuracy by using optimal weights that are upwind-biased. The use of large stencils in all circumstances, also makes those schemes not as robust as centrally-biased WENO schemes. Many of the more robust WENO schemes draw on the fundamental insight from Balsara and Shu [14] who found that the very higher order WENO schemes, because of their larger stencils, could be slightly unstable and, therefore, had to be stabilized with some monotonicity preserving process from smaller stencils. In that paper, the solution from the large, optimal, WENO stencil was non-linearly limited to lie within bounds provided by lower order monotonicity preserving polynomials derived from smaller stencils. The central WENO (CWENO) schemes (Cravero & Semplice [30]), which have also been extended to unstructured meshes by Semplice, Coco & Russo [59] also derive their robustness from the inclusion of smaller stencils. However, please also see the very robust WENO-ZQ and WENO-AO schemes by Zhu and Qiu [72] and Balsara Garain and Shu [14] which have the same idea and appeared in the same timeframe. It is possible to view WENO schemes generally as ones that have: - i) optimal weights (Jiang and Shu [47], Balsara and Shu [4], Hu and Shu [44], Zhang and Shu [71], Zhu and Qiu [79,81], Zhang et al. [80]), ii) WENO schemes based on non-optimal linear weights and with a large, ENO-type total stencil (Friedrichs [38], Levy, Puppo and Russo [50], Käser and Iske [45]) and iii) WENO schemes based on non-optimal linear weights, but which at the same time have an optimally compact total stencil (Zhu and Qiu [72], Balsara Garain and Shu [14], Zhu and Qiu [73], Zhu et al. [74], Zhao et al. [75],

Cravero and Semplice [30], Dumbser et al. [36]). The latter two types of WENO schemes emphasize the central, and most stable, stencil over and above all the other stencils. Thus for smooth flow, the reconstruction strategy is designed to seek out the most accurate central stencil. For non-smooth flow, the smoothness indicators permit the reconstruction to pick out the smoothest one-sided stencil. Experience has shown that the third order CWENO scheme is extremely stable, rivaling the stability of TVD schemes. The third order CWENO schemes also preserve physical extrema if such extrema exist in the flow. It is, therefore, desirable to build the twin advantages of stability and ability to capture extrema into very high order schemes, as we shall discuss in the next paragraph.

In Balsara, Garain and Shu [14] we realized that we can make a non-linear hybridization between a large, centered, very high accuracy stencil and a third order WENO scheme that is nevertheless very stable and capable of capturing physically meaningful extrema. (In a previous work, Zhu and Qiu [72] had non-linearly hybridized a fifth order reconstruction polynomial with a Van Albada-like limiter to arrive at a scheme that is fifth order for smooth flow and second order TVD at discontinuities.) The advances in Zhu and Qiu [72] and Balsara, Garain and Shu [14] were made for finite difference WENO, yielding a class of adaptive order schemes that we call WENO-AO (for adaptive order). Thus, on a structured mesh, we arrived at a WENO-AO(5,3) scheme that is at best fifth order accurate by virtue of its centered stencil with five zones and is non-linearly hybridized with a blend of second degree polynomials. The process can be extended to arrive at a WENO-AO(7,3) scheme that is at best seventh order accurate by virtue of its centered stencil with seven zones and again non-linearly hybridized with a similar blend of second degree polynomials. In this paper we show how the same advances are transcribed to WENO schemes for unstructured meshes.

Please note that for unstructured meshes, there is no fundamental objection to having a WENO-AO(4,3) or WENO-AO(5,4,3) scheme. However, when going from one order to the next higher order, we have to inflate the large stencil that we use. We have simply found it more economical to increase the order of the inflated large stencil in steps of two to arrive at WENO-AO(5,3) scheme schemes on unstructured meshes. As a result, the WENO-AO schemes designed here for unstructured meshes draw on the same two advances that made it possible to have WENO-AO schemes for structured meshes. First, we use a special basis set which is very easy to evaluate and which reduces the reconstruction of the solution on any given stencil to a least squares problem, instead of a constrained least squares problem. Instead of solving a constrained least squares problem, our method only requires the solution of a smaller least squares problem on each stencil. This also simplifies the matrix assembly and solution for each stencil. The evaluation of smoothness indicators is also simplified. Second, we use a non-linear hybridization of a very high order central stencil with a third order WENO scheme which is very stable. The large, centered, and very high accuracy stencil could keep local smooth extrema and lower accuracy stencils could keep essentially non-oscillatory property near strong discontinuities.

It is also worth noting that the CWENO methods suggested by Dumbser and Käser [34] tend to be very expensive because of the large number of characteristic projections that one has to carry out in directions that are orthogonal to all the faces of a given triangle or tetrahedron. For two dimensions, this entails three sets of characteristic projections for each of the zones that make up all of the stencils. For three dimensions, the number of characteristic projections increases to four. We find this to be prohibitively expensive for practical use. For that reason, we suggest the use of positivity considerations drawn from Balsara [11] to avoid the large number of characteristic projections. We find that when the reconstruction is based on non-linear hybridization and the need to retain positivity of density and pressure, the resulting scheme does not need characteristic projection. Instead, a reconstruction of the conserved variables is sufficient.

Section 2 describes the WENO reconstruction process as it has been extended to unstructured meshes using our current innovations. Section 3 describes the WENO-AO schemes at higher orders. Section 4 talks about simplifications that can be obtained on spherical meshes. Section 5 a brief synopsis of implementation-related details. Section 6 documents the order property for multidimensional test problems. Section 7 presents several stringent test problems. Section 8 draws some conclusions.

2. Third order WENO reconstruction on unstructured meshes

First we describe conventional, third order WENO reconstruction on an unstructured mesh. While the description in this section focuses on two-dimensions, it extends naturally to three dimensions. (Appendix A of this paper provides the details for three-dimensional WENO reconstruction.) The first purpose of this description is to show that when viewed in the Taylor basis that we present in this section, the third order WENO reconstruction even on unstructured meshes becomes very simple. The second purpose for this description stems from the fact that this WENO formulation will subsequently be used as a building block for the design of higher order WENO-AO schemes. We will use a central stencil and three forward sectorial stencils, as shown in Fig. 1. Notice that at third order, the number of degrees of freedom in 2D is given by $N_{dof} = 5$. As a result, our central stencil in Fig. 1b has $\sim 2N_{dof}$ zones; and our one-sided stencils in Figs. 1c, 1d and 1e have $\geq 1.5N_{dof}$ zones. This is in keeping with the suggestion from Dumbser and Käser [34] who find that the least squares minimization requires an overdetermined linear system, and that the system should be overdetermined by a certain small multiplicative factor. (Fig. 1a will be used in a later discussion.) A non-linear hybridization will eventually be made with the central stencil having a much larger linear weight and the three one-sided forward sectorial stencils having a much smaller linear weights.

Our choice of basis is inspired by the moments of inertia that are used in physics and engineering mechanics to describe the motion of rigid bodies. In those foundational subjects one learns that it is possible to develop a moment of inertia about a centroidal point of a solid body. Then the moment of inertia about any other point is given by that same moment

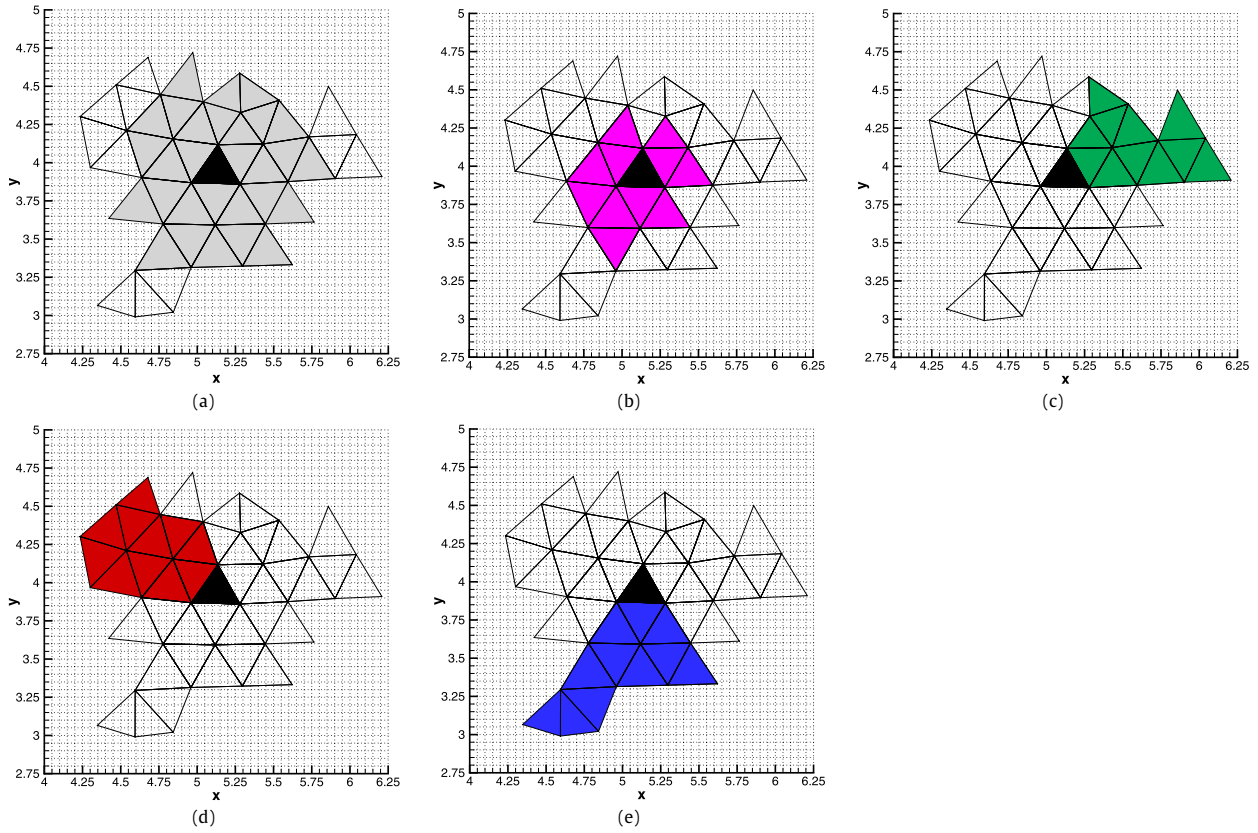

Fig. 1. Shows the five stencils that are used for fifth order WENO-AO on a two-dimensional unstructured mesh. The target zone in which the reconstruction is desired in shown in black. Fig. 1a shows the large central fifth order stencil. Fig. 1b shows the smaller central third order stencil. Figs. 1c, 1d and 1e show the smaller forward sectorial stencils at third order which are one-sided relative to the vertices of the target zone. Figs. 1b, 1c, 1d and 1e can also be used by themselves for a third order WENO reconstruction.

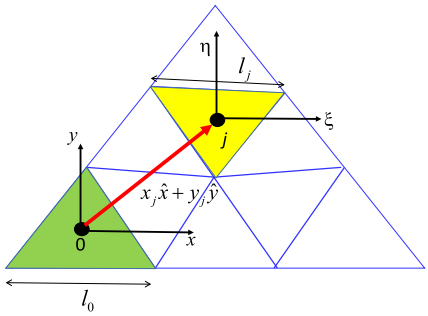

Fig. 2. Shows a stencil associated with the (green) zone "0" in thin lines. We consider the process of assembling one row of the least squares matrix for this stencil. The row concerns the (yellow) zone "j" in the stencil. The local coordinates for zone "0" are shown as (x, y) and the local coordinates for zone "j" are shown as (ξ, η). The centroids (center of masses) of the two zones are shown as heavy dots; the relative separation between the centroids is shown by the red vector. (For interpretation of the colors in the figure(s), the reader is referred to the web version of this article.)

about the centroid plus the mass of the body times the square of the distance to the centroid. (In classical mechanics, this is known as the Parallel Axis Theorem or the Huygens-Steiner Theorem, see Haas [41] or Goldstein et al. [40] for instance. Note though that in this paper we make a significant extension of the theorem without which it would not be useful for computational work.) The same simple idea is generalized in this paper to arrive at a favorable basis set that is based on the moments of inertia for each zone of the mesh. Only the first basis function has a non-zero mean value and corresponds to the zone-averaged conserved variable in the zone. The rest of the higher basis functions have zero mean when integrated over the element of interest. Such a basis is sometimes referred to as a Taylor basis (Luo et al. [53]). At third and higher orders it becomes easy to see the benefits of using the Taylor basis in conjunction with our generalization of the Parallel Axis Theorem, which is why this section introduces the idea at third order.

Consider the stencil that is shown in Fig. 2. It pertains to zone "0". We wish to reconstruct the moments in zone "0" using the other zones in the stencil. Let us consider the zone "j" which is within the shown stencil for zone "0". Let (x, y) be the local coordinate system located at zone "0". In other words, we locate the origin of our coordinate system at the centroid of zone "0". Let (ξ, η) be the local coordinate system for zone "j" whose centroid is located at a position $x_j\hat{x} + y_j\hat{y}$ relative to the zone "0". The displacement vector from zone "0" to zone "j" is shown by the red arrow in Fig. 2. Consequently, we can relate the coordinates within the two zones by the equations $x = x_j + \xi$ and $y = y_j + \eta$. For the zone "0" we would like to make the third order reconstruction that looks like

$$u^0(x,y) = \bar{u}^0 + \bar{u}^0_x x + \bar{u}^0_y y + \bar{u}^0_{xx}(x^2 - \bar{C}^0_{xx}) + \bar{u}^0_{yy}(y^2 - \bar{C}^0_{yy}) + \bar{u}^0_{xy}(xy - \bar{C}^0_{xy}) \tag{2.1}$$

Here $\bar{u}^0$ is the mean value of the conserved variable in zone "0" and is held fixed; the other moments of the conserved variables have to be reconstructed or evolved with limiting depending on the scheme used. The mesh (x, y) is located at the centroid of zone "0" with the result that the first geometric moments are zero. The second (and higher) geometric/physical moments, $\bar{C}^0_{xx}$, $\bar{C}^0_{yy}$ and $\bar{C}^0_{xy}$ for zone "0" can be obtained from

$$\bar{C}^0_{xx} = \frac{1}{|\Delta_0|}\iint\limits_{\Delta_0} x^2\,dx\,dy; \qquad \bar{C}^0_{yy} = \frac{1}{|\Delta_0|}\iint\limits_{\Delta_0} y^2\,dx\,dy; \qquad \bar{C}^0_{xy} = \frac{1}{|\Delta_0|}\iint\limits_{\Delta_0} xy\,dx\,dy; \quad \text{with } |\Delta_0| \equiv \iint\limits_{\Delta_0} dx\,dy \tag{2.2}$$

For the zone "j", *in principle*, the analogous reconstruction would look like

$$u^j(\xi,\eta) = \bar{u}^j + \bar{u}^j_x \xi + \bar{u}^j_y \eta + \bar{u}^j_{xx}(\xi^2 - \bar{C}^j_{xx}) + \bar{u}^j_{yy}(\eta^2 - \bar{C}^j_{yy}) + \bar{u}^j_{xy}(\xi\eta - \bar{C}^j_{xy}) \tag{2.3}$$

The second (and higher) geometric moments, $\bar{C}^j_{xx}$, $\bar{C}^j_{yy}$ and $\bar{C}^j_{xy}$ for zone "j" can be obtained as

$$\bar{C}^j_{xx} = \frac{1}{|\Delta_j|}\iint\limits_{\Delta_j} \xi^2\,d\xi\,d\eta; \qquad \bar{C}^j_{yy} = \frac{1}{|\Delta_j|}\iint\limits_{\Delta_j} \eta^2\,d\xi\,d\eta; \qquad \bar{C}^j_{xy} = \frac{1}{|\Delta_j|}\iint\limits_{\Delta_j} \xi\eta\,d\xi\,d\eta; \quad \text{where } |\Delta_j| \equiv \iint\limits_{\Delta_j} d\xi\,d\eta \tag{2.4}$$

The geometric moments, $\bar{C}^j_{xx}$, $\bar{C}^j_{yy}$ and $\bar{C}^j_{xy}$, in zone "j" will play an important role in the efficient reconstruction of the conserved variables in zone "0". Later on, we will see that the fluid moments $\bar{u}^j_x$, $\bar{u}^j_y$, $\bar{u}^j_{xx}$, $\bar{u}^j_{yy}$ and $\bar{u}^j_{xy}$ will not be needed when making finite volume WENO reconstruction in zone "0". Similarly, even though this is not the goal of this paper, if we are perhaps making P1PN reconstruction, we will see that the moments $\bar{u}^j_{xx}$, $\bar{u}^j_{yy}$ and $\bar{u}^j_{xy}$ will not be needed when reconstructing the quadratic terms in eqn. (2.1).

Eqns. (2.1) and (2.3), despite their utility as intermediate equations, will not be used directly in a computer implementation. The two good reasons for this decision are as follows:

1) In general we may have zones of vastly different sizes close to one another. This happens quite frequently on an unstructured mesh. This unfavorable juxtaposition of zone sizes can sometimes result in poorly conditioned matrices.
2) We want to obtain as much concordance as we can to the structured mesh WENO, where we know and understand how to seamlessly construct smoothness indicators. The weight of experience, derived from structured meshes, is that it helps to regularize each zone to be a unit interval. We would like to do the same for unstructured meshes because it will help us in defining smoothness indicators.

Let us, therefore, take steps to overcome these two deficiencies from the very onset. Let zone "0" have a characteristic length l_0 as shown in the figure and let zone "j" have a characteristic length l_j as shown in Fig. 2. We can then rewrite eqn. (2.1) in zone "0" using coordinates that are scaled by the length l_0 as

$$u^0(x,y) = \bar{u}^0 + u^0_x\left(\frac{x}{l_0}\right) + u^0_y\left(\frac{y}{l_0}\right) + u^0_{xx}\left[\left(\frac{x}{l_0}\right)^2 - C^0_{xx}\right] + u^0_{yy}\left[\left(\frac{y}{l_0}\right)^2 - C^0_{yy}\right] + u^0_{xy}\left[\left(\frac{x}{l_0}\right)\left(\frac{y}{l_0}\right) - C^0_{xy}\right] \tag{2.5}$$

We can analogously write eqn. (2.3) for the zone "j" using coordinates that are scaled by the length l_j as

$$u^j(\xi,\eta) = \bar{u}^j + u^j_x\left(\frac{\xi}{l_j}\right) + u^j_y\left(\frac{\eta}{l_j}\right) + u^j_{xx}\left[\left(\frac{\xi}{l_j}\right)^2 - C^j_{xx}\right] + u^j_{yy}\left[\left(\frac{\eta}{l_j}\right)^2 - C^j_{yy}\right] + u^j_{xy}\left[\left(\frac{\xi}{l_j}\right)\left(\frac{\eta}{l_j}\right) - C^j_{xy}\right] \tag{2.6}$$

Taking eqns. (2.5) and (2.6) as an examples, we have the following rescaling of the modes and the geometrical moments

$$\begin{aligned}
&u^0_x = \bar{u}^0_x l_0; \quad u^0_y = \bar{u}^0_y l_0; \quad u^0_{xx} = \bar{u}^0_{xx} l_0^2; \quad u^0_{yy} = \bar{u}^0_{yy} l_0^2; \quad u^0_{xy} = \bar{u}^0_{xy} l_0^2;\\
&u^j_x = \bar{u}^j_x l_j; \quad u^j_y = \bar{u}^j_y l_j; \quad u^j_{xx} = \bar{u}^j_{xx} l_j^2; \quad u^j_{yy} = \bar{u}^j_{yy} l_j^2; \quad u^j_{xy} = \bar{u}^j_{xy} l_j^2;\\
&C^0_{xx} = \frac{\bar{C}^0_{xx}}{l_0^2}; \quad C^0_{yy} = \frac{\bar{C}^0_{yy}}{l_0^2}; \quad C^0_{xy} = \frac{\bar{C}^0_{xy}}{l_0^2}; \quad C^j_{xx} = \frac{\bar{C}^j_{xx}}{l_j^2}; \quad C^j_{yy} = \frac{\bar{C}^j_{yy}}{l_j^2}; \quad C^j_{xy} = \frac{\bar{C}^j_{xy}}{l_j^2}
\end{aligned} \tag{2.7}$$

Eqns. (2.5) and (2.6), along with the rescaling in eqn. (2.7), are in a format that is suitable for computer usage. However, please note that eqns. (2.1) and (2.3) are very useful for deriving the mathematical relations. In other words, eqns. (2.1) to (2.4) and (2.7) are essential in helping to define the moments and showing the reader the steps that go into the exact evaluation and rescaling of those moments. However, in most codes this definition and rescaling of the moments only needs to be carried out and stored only once. After than is done, the reconstruction relies on the scaled equations given by eqns. (2.5) and (2.6). The only exception would be Lagrangian or ALE type codes where the mesh topology keeps changing every timestep; where the moments would need to be regenerated at every timestep.

The stencil shown in Fig. 2 has eight zones other than the zone "0". As a result, we will obtain a least squares matrix with eight rows for this particular stencil; furthermore, the matrix will have $N_{dof} = 5$ number of columns. Let us focus on specifying how each row of that least squares matrix is constructed. Each zone "j" in the stencil shown in Fig. 2 will provide one row for the least squares matrix. In constructing any row of the least squares matrix (for the stencil shown in Fig. 2), we will have to assert the following requirement

$$\bar{u}_j = \frac{1}{|\Delta_j|} \iint\limits_{\Delta_j} u^0(x, y)\, dx\, dy \tag{2.8}$$

By making the coordinate transformation

$$\xi = x - x_j; \qquad \eta = y - y_j \tag{2.9}$$

we can write eqn. (2.8) in terms of the local coordinates associated with zone "j" as follows

$$\bar{u}_j = \frac{1}{|\Delta_j|} \iint\limits_{\Delta_j} u^0(\xi + x_j, \eta + y_j)\, d\xi\, d\eta \tag{2.10}$$

Consequently, we can write

$$\begin{aligned} u^0(\xi + x_j, \eta + y_j) = \bar{u}^0 + \bar{u}^0_x(\xi + x_j) + \bar{u}^0_y(\eta + y_j) + \bar{u}^0_{xx}\big[(\xi + x_j)^2 - \bar{C}^0_{xx}\big] \\ + \bar{u}^0_{yy}\big[(\eta + y_j)^2 - \bar{C}^0_{yy}\big] + \bar{u}^0_{xy}\big[(\xi + x_j)(\eta + y_j) - \bar{C}^0_{xy}\big] \end{aligned} \tag{2.11}$$

This is where the idea of shifting the physical moments, drawn from classical mechanics and the Parallel Axis Theorem, becomes very useful. We illustrate it explicitly for the following integral

$$\begin{aligned} \iint\limits_{\Delta_j} \big[(\xi + x_j)^2 - \bar{C}^0_{xx}\big] d\xi\, d\eta &= \iint\limits_{\Delta_j} \big[x_j^2 - \bar{C}^0_{xx} + 2x_j\xi + \xi^2\big] d\xi\, d\eta = |\Delta_j|\big[x_j^2 - \bar{C}^0_{xx}\big] + |\Delta_j|\bar{C}^j_{xx} \\ &= |\Delta_j| l_0^2 \left\{ \left[\left(\frac{x_j}{l_0} \right)^2 - C^0_{xx} \right] + \left(\frac{l_j}{l_0} \right)^2 C^j_{xx} \right\} \end{aligned} \tag{2.12}$$

Analogously to eqn. (2.12), we can write the remaining two integrals without providing intermediate steps as follows

$$\iint\limits_{\Delta_j} \big[(\eta + y_j)^2 - \bar{C}^0_{yy}\big] d\xi\, d\eta = |\Delta_j| l_0^2 \left\{ \left[\left(\frac{y_j}{l_0} \right)^2 - C^0_{yy} \right] + \left(\frac{l_j}{l_0} \right)^2 C^j_{yy} \right\} \tag{2.13}$$

and

$$\iint\limits_{\Delta_j} \big[(\xi + x_j)(\eta + y_j) - \bar{C}^0_{xy}\big] d\xi\, d\eta = |\Delta_j| l_0^2 \left\{ \left[\left(\frac{x_j}{l_0} \right)\left(\frac{y_j}{l_0} \right) - C^0_{xy} \right] + \left(\frac{l_j}{l_0} \right)^2 C^j_{xy} \right\} \tag{2.14}$$

The above three equations show how the integrals in eqn. (2.10) are quickly and easily evaluated. The simplicity in the evaluation is a direct byproduct of our generalization of the Parallel Axis Theorem.

We now wish to assemble the desired row of the least squares matrix associated with Fig. 2. The row of the least squares matrix that corresponds to triangle "j" is then given by

$$\begin{aligned} &u^0_x \left[\left(\frac{x_j}{l_0} \right) \right] + u^0_y \left[\left(\frac{y_j}{l_0} \right) \right] + u^0_{xx} \left[\left(\frac{x_j}{l_0} \right)^2 - C^0_{xx} + \left(\frac{l_j}{l_0} \right)^2 C^j_{xx} \right] \\ &+ u^0_{yy} \left[\left(\frac{y_j}{l_0} \right)^2 - C^0_{yy} + \left(\frac{l_j}{l_0} \right)^2 C^j_{yy} \right] + u^0_{xy} \left[\left(\frac{x_j}{l_0} \right)\left(\frac{y_j}{l_0} \right) - C^0_{xy} + \left(\frac{l_j}{l_0} \right)^2 C^j_{xy} \right] = \bar{u}^j - \bar{u}^0 \end{aligned} \tag{2.15}$$

Such an equation is very easy to evaluate/assemble and can be asserted for each of the eight zones in the stencil shown in Fig. 2. Doing this for each of the elements in Fig. 2 enables us to assemble the entire least squares matrix. The right hand

side of eqn. (2.15) gives us one of the elements of the right hand side vector for the least squares system. Please realize that all the physical moments in eqn. (2.15) are evaluated only once at the beginning of the simulation and are stored at each of the zones. As a result, the assembly of the coefficients in eqn. (2.15) is nearly automatic. Each zone stores a list of zones that participate in each of its four, third-order stencils, shown in Fig. 1. In [59] a similar transcription from constrained least squares to unconstrained least squares was shown for structured meshes; however, this paper shows that achieving analogous transcription for unstructured meshes is substantially more complicated.

For the above formula to work, however, please note that the geometrical moments for any zone have to be constructed relative to the centroid of that zone. Of course, the geometrical moments should be constructed with third or better order of accuracy using suitably accurate quadrature points. It is also important to realize that the method does not distinguish between element shape; the elements can be triangles or tetrahedra or polygons in 2D; or the elements can be tetrahedra or hexahedra or polyhedra in 3D. Furthermore, as long as suitably accurate quadrature is used, the elements can have curved sides or even curved surfaces in 3D. This highlights the incredible utility and flexibility of the method proposed here. As long as the physical moments are accurately evaluated and stored for each zone, the entire reconstruction takes place in physical space. In an ALE calculation, where the vertices of the mesh can move, one has of course to evaluate the moments at every timestep. But in all other circumstances, the moments should only be evaluated and stored once and reused in subsequent timesteps.

Now that we have the modes of the reconstruction for each of the four stencils of interest, we can define smoothness indicators for all the stencils. The smoothness indicator for each stencil is given by

$$\beta = \left(u_x^0\right)^2 + \left(u_y^0\right)^2 + \left(u_{xx}^0\right)^2 + \left(u_{yy}^0\right)^2 + \left(u_{xy}^0\right)^2 \tag{2.16}$$

The above definition of the smoothness indicators, because it is correctly scaled for zone size (see eqn. (2.17)) retains the spirit of the smoothness indicators in Jiang and Shu [47] and, of course, our simplified smoothness indicators have the advantage that they are easier to evaluate. Our practical experience is that they work very well because of the suitable scaling; however, other choices of scaling can always be made. Notice that if we refer to the stencil in Fig. 1b as stencil number 1 and if we refer to the other three one-sided stencils in Figs. 1c, 1d and 1e as stencils number 2, 3 and 4 then we have four smoothness indicators β_1, β_2, β_3 and β_4. We can then write the non-linear weights as

$$w_1 = \frac{\gamma_C}{(\beta_1+\varepsilon)^s}; \qquad w_2 = \frac{1}{(\beta_2+\varepsilon)^s}; \qquad w_3 = \frac{1}{(\beta_3+\varepsilon)^s}; \qquad w_4 = \frac{1}{(\beta_4+\varepsilon)^s} \tag{2.17}$$

We then obtain the normalized non-linear weights as

$$\begin{aligned} \bar{w}_1 &= \frac{w_1}{w_1+w_2+w_3+w_4}; \\ \bar{w}_2 &= \frac{w_2}{w_1+w_2+w_3+w_4}; \qquad \bar{w}_3 = \frac{w_3}{w_1+w_2+w_3+w_4}; \qquad \bar{w}_4 = \frac{w_4}{w_1+w_2+w_3+w_4} \end{aligned} \tag{2.18}$$

Following Dumbser and Käser [34] we choose $s = 4$, $\varepsilon = 10^{-12}$ and $\gamma_C \in [50, 400]$. The modes from the different stencils can be non-linearly hybridized using the normalized non-linear weights in eqn. (2.18). Therefore, let $R^{p2;1}(x, y)$ denote the two-dimensional reconstructed polynomial associated with the central stencil; it will have a quadratic form analogous to eqn. (2.5). Let $R^{p2;2}(x, y)$, $R^{p2;3}(x, y)$ and $R^{p2;4}(x, y)$ denote the two-dimensional reconstructed polynomials associated with the three one-sided stencils; they too will have a quadratic form analogous to eqn. (2.5). The superscript "$p2$" in the above nomenclature for the reconstructed polynomials indicates that the polynomials are quadratic in their variation. The final, non-linearly hybridized WENO reconstruction at third order is given by

$$R^{WENO}(x, y) = \bar{w}_1 R^{p2;1}(x, y) + \bar{w}_2 R^{p2;2}(x, y) + \bar{w}_3 R^{p2;3}(x, y) + \bar{w}_4 R^{p2;4}(x, y) \tag{2.19}$$

This completes our description of the third order WENO reconstruction for unstructured meshes. The extension to 3D meshes is transparent. The method can be combined with a third order evaluation of the fluxes at the zone boundaries using any suitable Riemann solver. Each stage in the update can be combined with an SSP-RK strategy for achieving high order of temporal accuracy to achieve a scheme that is third order accurate in space and time.

3. Higher order WENO-AO reconstruction on unstructured meshes

The previous section showed us how the geometric/physical moments can be used to obtain a WENO reconstruction strategy that only uses least squares minimization rather than constrained least squares minimization. We also showed how it simplifies the definition of the smoothness indicators. The WENO reconstruction in the previous section was restricted to third order of accuracy. In this section we show that the process extends to fourth and fifth orders of accuracy.

This section is split into three sub-sections. Sub-section 3.1 shows how the previous procedure can be extended to the reconstruction of a fourth order central stencil. Sub-section 3.2 provides some further helpful details for fifth order accurate reconstruction of a central stencil. Sub-section 3.3 shows how WENO-AO schemes can be formulated using the mathematics that we develop in this section.

3.1. Fourth order central stencil reconstruction for unstructured meshes

At fourth order, the analogue of eqn. (2.1) becomes

$$\begin{aligned} u^0(x,y) = \bar{u}^0 &+ \bar{u}^0_x x + \bar{u}^0_y y + \bar{u}^0_{xx}(x^2 - \bar{C}^0_{xx}) + \bar{u}^0_{yy}(y^2 - \bar{C}^0_{yy}) + \bar{u}^0_{xy}(xy - \bar{C}^0_{xy}) \\ &+ \bar{u}^0_{xxx}(x^3 - \bar{C}^0_{xxx}) + \bar{u}^0_{yyy}(y^3 - \bar{C}^0_{yyy}) + \bar{u}^0_{xxy}(x^2 y - \bar{C}^0_{xxy}) + \bar{u}^0_{xyy}(xy^2 - \bar{C}^0_{xyy}) \end{aligned} \tag{3.1}$$

Just like eqn. (2.2) we define

$$\bar{C}^0_{xxx} = \frac{1}{|\Delta_0|}\iint\limits_{\Delta_0} x^3\,dx\,dy; \quad \bar{C}^0_{yyy} = \frac{1}{|\Delta_0|}\iint\limits_{\Delta_0} y^3\,dx\,dy; \quad \bar{C}^0_{xxy} = \frac{1}{|\Delta_0|}\iint\limits_{\Delta_0} x^2 y\,dx\,dy; \quad \bar{C}^0_{xyy} = \frac{1}{|\Delta_0|}\iint\limits_{\Delta_0} xy^2\,dx\,dy \tag{3.2}$$

Note though that while the integrals in eqn. (2.2) could be evaluated with third order accuracy for third order accurate WENO, the fourth order WENO requires more accuracy. Consequently, for fourth order WENO, the integrals in eqns. (3.2) as well as (2.2) have to be evaluated with fourth order accuracy. Furthermore, if the element has curved faces, the centroid might have to be evaluated numerically. In that case, the centroid evaluation should also be done with fourth or higher order accuracy. For the sake of brevity, we will not repeat analogous information for eqns. (2.3) and (2.4).

For a computer implementation we will need the analogue of eqn. (2.5) which is given as

$$\begin{aligned} u^0(x,y) = \bar{u}^0 &+ u^0_x\left(\frac{x}{l_0}\right) + u^0_y\left(\frac{y}{l_0}\right) + u^0_{xx}\left[\left(\frac{x}{l_0}\right)^2 - C^0_{xx}\right] + u^0_{yy}\left[\left(\frac{y}{l_0}\right)^2 - C^0_{yy}\right] + u^0_{xy}\left[\left(\frac{x}{l_0}\right)\left(\frac{y}{l_0}\right) - C^0_{xy}\right] \\ &+ u^0_{xxx}\left[\left(\frac{x}{l_0}\right)^3 - C^0_{xxx}\right] + u^0_{yyy}\left[\left(\frac{y}{l_0}\right)^3 - C^0_{yyy}\right] + u^0_{xxy}\left[\left(\frac{x}{l_0}\right)^2\left(\frac{y}{l_0}\right) - C^0_{xxy}\right] \\ &+ u^0_{xyy}\left[\left(\frac{x}{l_0}\right)\left(\frac{y}{l_0}\right)^2 - C^0_{xyy}\right] \end{aligned} \tag{3.3}$$

In addition to the rescaling in eqn. (2.7), we also have

$$\begin{aligned} &u^0_{xxx} = \bar{u}^0_{xxx} l_0^3; \quad u^0_{yyy} = \bar{u}^0_{yyy} l_0^3; \quad u^0_{xxy} = \bar{u}^0_{xxy} l_0^3; \quad u^0_{xyy} = \bar{u}^0_{xyy} l_0^3; \\ &C^0_{xxx} = \frac{\bar{C}^0_{xxx}}{l_0^3}; \quad C^0_{yyy} = \frac{\bar{C}^0_{yyy}}{l_0^3}; \quad C^0_{xxy} = \frac{\bar{C}^0_{xxy}}{l_0^3}; \quad C^0_{xyy} = \frac{\bar{C}^0_{xyy}}{l_0^3} \end{aligned} \tag{3.4}$$

Analogous to eqns. (2.12), (2.13) and (2.14), at fourth order we have

$$\iint\limits_{\Delta_j} \left[(\xi + x_j)^3 - \bar{C}^0_{xxx}\right] d\xi\,d\eta = |\Delta_j| l_0^3 \left\{\left[\left(\frac{x_j}{l_0}\right)^3 - C^0_{xxx}\right] + 3\left(\frac{x_j}{l_0}\right)\left(\frac{l_j}{l_0}\right)^2 C^j_{xx} + \left(\frac{l_j}{l_0}\right)^3 C^j_{xxx}\right\} \tag{3.5}$$

and

$$\iint\limits_{\Delta_j} \left[(\eta + y_j)^3 - \bar{C}^0_{yyy}\right] d\xi\,d\eta = |\Delta_j| l_0^3 \left\{\left[\left(\frac{y_j}{l_0}\right)^3 - C^0_{yyy}\right] + 3\left(\frac{y_j}{l_0}\right)\left(\frac{l_j}{l_0}\right)^2 C^j_{yy} + \left(\frac{l_j}{l_0}\right)^3 C^j_{yyy}\right\} \tag{3.6}$$

and

$$\begin{aligned} &\iint\limits_{\Delta_j} \left[(\xi + x_j)^2(\eta + y_j) - \bar{C}^0_{xxy}\right] d\xi\,d\eta \\ &= |\Delta_j| l_0^2 \left\{\left[\left(\frac{x_j}{l_0}\right)^2\left(\frac{y_j}{l_0}\right) - C^0_{xxy}\right] + \left(\frac{y_j}{l_0}\right)\left(\frac{l_j}{l_0}\right)^2 C^j_{xx} + 2\left(\frac{x_j}{l_0}\right)\left(\frac{l_j}{l_0}\right)^2 C^j_{xy} + \left(\frac{l_j}{l_0}\right)^3 C^j_{xxy}\right\} \end{aligned} \tag{3.7}$$

and

$$\begin{aligned} &\iint\limits_{\Delta_j} \left[(\xi + x_j)(\eta + y_j)^2 - \bar{C}^0_{xyy}\right] d\xi\,d\eta \\ &= |\Delta_j| l_0^2 \left\{\left[\left(\frac{x_j}{l_0}\right)\left(\frac{y_j}{l_0}\right)^2 - C^0_{xyy}\right] + \left(\frac{x_j}{l_0}\right)\left(\frac{l_j}{l_0}\right)^2 C^j_{yy} + 2\left(\frac{y_j}{l_0}\right)\left(\frac{l_j}{l_0}\right)^2 C^j_{xy} + \left(\frac{l_j}{l_0}\right)^3 C^j_{xyy}\right\} \end{aligned} \tag{3.8}$$

Finally, we can write the analogue of eqn. (3.16) as

$$\begin{aligned}
&u^0_x\left[\left(\frac{x_j}{l_0}\right)\right] + u^0_y\left[\left(\frac{y_j}{l_0}\right)\right] + u^0_{xx}\left[\left(\frac{x_j}{l_0}\right)^2 - C^0_{xx} + \left(\frac{l_j}{l_0}\right)^2 C^j_{xx}\right] \\
&+ u^0_{yy}\left[\left(\frac{y_j}{l_0}\right)^2 - C^0_{yy} + \left(\frac{l_j}{l_0}\right)^2 C^j_{yy}\right] + u^0_{xy}\left[\left(\frac{x_j}{l_0}\right)\left(\frac{y_j}{l_0}\right) - C^0_{xy} + \left(\frac{l_j}{l_0}\right)^2 C^j_{xy}\right] \\
&+ u^0_{xxx}\left[\left(\frac{x_j}{l_0}\right)^3 - C^0_{xxx} + 3\left(\frac{x_j}{l_0}\right)\left(\frac{l_j}{l_0}\right)^2 C^j_{xx} + \left(\frac{l_j}{l_0}\right)^3 C^j_{xxx}\right] \\
&+ u^0_{yyy}\left[\left(\frac{y_j}{l_0}\right)^3 - C^0_{yyy} + 3\left(\frac{y_j}{l_0}\right)\left(\frac{l_j}{l_0}\right)^2 C^j_{yy} + \left(\frac{l_j}{l_0}\right)^3 C^j_{yyy}\right] \\
&+ u^0_{xxy}\left[\left(\frac{x_j}{l_0}\right)^2\left(\frac{y_j}{l_0}\right) - C^0_{xxy} + \left(\frac{y_j}{l_0}\right)\left(\frac{l_j}{l_0}\right)^2 C^j_{xx} + 2\left(\frac{x_j}{l_0}\right)\left(\frac{l_j}{l_0}\right)^2 C^j_{xy} + \left(\frac{l_j}{l_0}\right)^3 C^j_{xxy}\right] \\
&+ u^0_{xyy}\left[\left(\frac{x_j}{l_0}\right)\left(\frac{y_j}{l_0}\right)^2 - C^0_{xyy} + \left(\frac{x_j}{l_0}\right)\left(\frac{l_j}{l_0}\right)^2 C^j_{yy} + 2\left(\frac{y_j}{l_0}\right)\left(\frac{l_j}{l_0}\right)^2 C^j_{xy} + \left(\frac{l_j}{l_0}\right)^3 C^j_{xyy}\right] = \bar{u}^j - \bar{u}^0
\end{aligned} \tag{3.9}$$

The above equation gives us an explicit expression for one of the rows of the least squares matrix. The right hand side of eqn. (3.9) gives us one of the elements of the right hand side vector for the least squares system. For each different element in the stencil, we will get one more such row. This shows us how the least squares matrix is to be assembled. If sufficient memory is available in the computer, one can assemble the least squares matrix once and for all at the beginning of the computation for all the stencils that are to be used and for all the zones of the mesh. We realize, however, that this might be memory-intensive. (It is worth mentioning that the three-dimensional analogues of eqns. (3.5) to (3.8) have been given in Appendix A of this paper.)

Let $R^{p3;0}(x, y)$ denote the two-dimensional reconstructed polynomial associated with the large fourth order accurate central stencil described in this Sub-section. It will have a cubic form analogous to eqn. (3.3). Extending the smoothness indicator definition from eqn. (2.16) to the present section, we can write the smoothness indicator for the large central stencil as

$$\beta_0 = \left(u^0_x\right)^2 + \left(u^0_y\right)^2 + \left(u^0_{xx}\right)^2 + \left(u^0_{yy}\right)^2 + \left(u^0_{xy}\right)^2 + \left(u^0_{xxx}\right)^2 + \left(u^0_{yyy}\right)^2 + \left(u^0_{xxy}\right)^2 + \left(u^0_{xyy}\right)^2 \tag{3.10}$$

In Sub-section 3.3 we will show how a large, high order stencil can be non-linearly hybridized with smaller third order stencils from Section 2.

3.2. Fifth order central stencil reconstruction for unstructured meshes

Once the third and fourth order reconstruction strategies are described, the extension to all higher orders becomes rather transparent. Consequently, we do not present a lot of detail for the fifth order case. We only describe the parts that are somewhat difficult. The analogue of eqn. (3.3) now becomes

$$\begin{aligned}
u^0(x, y) = \bar{u}^0 &+ u^0_x\left(\frac{x}{l_0}\right) + u^0_y\left(\frac{y}{l_0}\right) + u^0_{xx}\left[\left(\frac{x}{l_0}\right)^2 - C^0_{xx}\right] + u^0_{yy}\left[\left(\frac{y}{l_0}\right)^2 - C^0_{yy}\right] + u^0_{xy}\left[\left(\frac{x}{l_0}\right)\left(\frac{y}{l_0}\right) - C^0_{xy}\right] \\
&+ u^0_{xxx}\left[\left(\frac{x}{l_0}\right)^3 - C^0_{xxx}\right] + u^0_{yyy}\left[\left(\frac{y}{l_0}\right)^3 - C^0_{yyy}\right] + u^0_{xxy}\left[\left(\frac{x}{l_0}\right)^2\left(\frac{y}{l_0}\right) - C^0_{xxy}\right] \\
&+ u^0_{xyy}\left[\left(\frac{x}{l_0}\right)\left(\frac{y}{l_0} - C^0_{xyy}\right)\right] + u^0_{xxxx}\left[\left(\frac{x}{l_0}\right)^4 - C^0_{xxxx}\right] \\
&+ u^0_{yyyy}\left[\left(\frac{y}{l_0}\right)^4 - C^0_{yyyy}\right] + u^0_{xxxy}\left[\left(\frac{x}{l_0}\right)^3\left(\frac{y}{l_0}\right) - C^0_{xxxy}\right] + u^0_{xyyy}\left[\left(\frac{x}{l_0}\right)\left(\frac{y}{l_0}\right)^3 - C^0_{xyyy}\right] \\
&+ u^0_{xxyy}\left[\left(\frac{x}{l_0}\right)^2\left(\frac{y}{l_0}\right)^2 - C^0_{xxyy}\right]
\end{aligned} \tag{3.11}$$

For the fifth order reconstruction, all the physical moments in eqn. (3.11) have to be evaluated with fifth or higher order accurate quadrature.

The only difficult part is the evaluation of the integrals. Analogous to eqns. (2.12), (2.13) and (2.14), and also analogous to eqns. (3.5), (3.6), (3.7) and (3.8), at fifth order we have

$$\iint\limits_{\Delta_j}\left[(\xi+x_j)^4-\bar{C}^0_{xxxx}\right]d\xi\,d\eta$$
$$=|\Delta_j|l_0^3\left\{\left[\left(\frac{x_j}{l_0}\right)^4-C^0_{xxxx}\right]+6\left(\frac{x_j}{l_0}\right)^2\left(\frac{l_j}{l_0}\right)^2C^j_{xx}+4\left(\frac{x_j}{l_0}\right)\left(\frac{l_j}{l_0}\right)^3C^j_{xxx}+\left(\frac{l_j}{l_0}\right)^4C^j_{xxxx}\right\} \tag{3.12}$$

and

$$\iint\limits_{\Delta_j}\left[(\eta+y_j)^4-\bar{C}^0_{yyyy}\right]d\xi\,d\eta$$
$$=|\Delta_j|l_0^3\left\{\left[\left(\frac{y_j}{l_0}\right)^4-C^0_{yyyy}\right]+6\left(\frac{y_j}{l_0}\right)^2\left(\frac{l_j}{l_0}\right)^2C^j_{yy}+4\left(\frac{y_j}{l_0}\right)\left(\frac{l_j}{l_0}\right)^3C^j_{yyy}+\left(\frac{l_j}{l_0}\right)^4C^j_{yyyy}\right\} \tag{3.13}$$

and

$$\iint\limits_{\Delta_j}\left[(\xi+x_j)^3(\eta+y_j)-\bar{C}^0_{xxxy}\right]d\xi\,d\eta$$
$$=|\Delta_j|l_0^3\left\{\begin{array}{l}\left[\left(\frac{x_j}{l_0}\right)^3\left(\frac{y_j}{l_0}\right)-C^0_{xxxy}\right]+3\left(\frac{x_j}{l_0}\right)\left(\frac{y_j}{l_0}\right)\left(\frac{l_j}{l_0}\right)^2C^j_{xx}+3\left(\frac{x_j}{l_0}\right)^2\left(\frac{l_j}{l_0}\right)^2C^j_{xy}\\ \quad+\left(\frac{y_j}{l_0}\right)\left(\frac{l_j}{l_0}\right)^3C^j_{xxx}+3\left(\frac{x_j}{l_0}\right)\left(\frac{l_j}{l_0}\right)^3C^j_{xxy}+\left(\frac{l_j}{l_0}\right)^4C^j_{xxxy}\end{array}\right\} \tag{3.14}$$

and

$$\iint\limits_{\Delta_j}\left[(\xi+x_j)(\eta+y_j)^3-\bar{C}^0_{xyyy}\right]d\xi\,d\eta$$
$$=|\Delta_j|l_0^3\left\{\begin{array}{l}\left[\left(\frac{x_j}{l_0}\right)\left(\frac{y_j}{l_0}\right)^3-C^0_{xyyy}\right]+3\left(\frac{x_j}{l_0}\right)\left(\frac{y_j}{l_0}\right)\left(\frac{l_j}{l_0}\right)^2C^j_{yy}+3\left(\frac{y_j}{l_0}\right)^2\left(\frac{l_j}{l_0}\right)^2C^j_{xy}\\ \quad+\left(\frac{x_j}{l_0}\right)\left(\frac{l_j}{l_0}\right)^3C^j_{yyy}+3\left(\frac{y_j}{l_0}\right)\left(\frac{l_j}{l_0}\right)^3C^j_{xyy}+\left(\frac{l_j}{l_0}\right)^4C^j_{xyyy}\end{array}\right\} \tag{3.15}$$

and

$$\iint\limits_{\Delta_j}\left[(\xi+x_j)^2(\eta+y_j)^2-\bar{C}^0_{xxyy}\right]d\xi\,d\eta$$
$$=|\Delta_j|l_0^3\left\{\begin{array}{l}\left[\left(\frac{x_j}{l_0}\right)^2\left(\frac{y_j}{l_0}\right)^2-C^0_{xxyy}\right]+\left(\frac{y_j}{l_0}\right)^2\left(\frac{l_j}{l_0}\right)^2C^j_{xx}+\left(\frac{x_j}{l_0}\right)^2\left(\frac{l_j}{l_0}\right)^2C^j_{yy}\\ \quad+4\left(\frac{x_j}{l_0}\right)\left(\frac{y_j}{l_0}\right)\left(\frac{l_j}{l_0}\right)^2C^j_{xy}+2\left(\frac{y_j}{l_0}\right)\left(\frac{l_j}{l_0}\right)^3C^j_{xxy}+2\left(\frac{x_j}{l_0}\right)\left(\frac{l_j}{l_0}\right)^3C^j_{xyy}+\left(\frac{l_j}{l_0}\right)^4C^j_{xxyy}\end{array}\right\} \tag{3.16}$$

The above five equations make it very easy to assemble the rows in the least squares matrix for fifth order accurate reconstruction when it is applied to the central stencil. Fig. 1a shows a representative the fifth order accurate central stencil in two dimensions. Fig. 1a helps us to appreciate that the fifth order WENO-AO will only require us to include one further stencil in addition to the four third order stencils shown in Figs. 1b, 1c, 1d and 1e. As a result, the fifth order WENO-AO formulation is not substantially more expensive as compared to the third order formulation.

Let $R^{p4;0}(x,y)$ denote the two-dimensional reconstructed polynomial associated with the large fifth order accurate central stencil described in this Sub-section. It will have a quartic form analogous to eqn. (3.11). Extending the smoothness indicator definition from eqn. (3.10) to the present section, we can write the smoothness indicator for the large central stencil as

$$\begin{aligned}\beta_0=&\left(u^0_x\right)^2+\left(u^0_y\right)^2+\left(u^0_{xx}\right)^2+\left(u^0_{yy}\right)^2+\left(u^0_{xy}\right)^2+\left(u^0_{xxx}\right)^2+\left(u^0_{yyy}\right)^2+\left(u^0_{xxy}\right)^2+\left(u^0_{xyy}\right)^2\\&+\left(u^0_{xxxx}\right)^2+\left(u^0_{yyyy}\right)^2+\left(u^0_{xxxy}\right)^2+\left(u^0_{xyyy}\right)^2+\left(u^0_{xxyy}\right)^2\end{aligned} \tag{3.17}$$

In Sub-section 3.3 we will show how a large, high order stencil can be non-linearly hybridized with smaller third order stencils from Section 2.

3.3. Assembling WENO-AO schemes

The details of this non-linear hybridization for WENO-AO(5,3) will be described in the next paragraph. However, it is very important to mention that the intuitive underpinnings of this method derive from the recent, and very nice, paper by Zhu and Qiu [72], who hybridized the fifth order central stencil and a Van Albada-type of limiter on a structured mesh. The Van Albada limiter is a TVD-class limiter which can clip extrema. For that reason, it is more advisable to nonlinearly hybridize the scheme with a suitable third order CWENO scheme as was done by Balsara, Garain and Shu [14] also for structured meshes; see also [72]. Our goal in this section is to extend WENO-AO(5,3) to unstructured meshes.

Now let us focus on a detailed description of WENO-AO(5,3). This description is important because we will later on show that it can also open the door to other families of WENO-AO schemes. The method is described by two parameters, γ_{Hi} and γ_{Lo}, both of which are always positive and less than unity. The linear weight for the large (fifth order) central stencil is denoted by γ_0; the linear weight for the smaller (third order) central stencil is denoted by γ_1; and the linear weights of the three one-sided (third order) stencils are denoted by γ_2, γ_3 and γ_4. The construction of the fifth order stencil is described in Sub-section 3.2 and the construction of the smaller third order stencils is described in Section 2. The linear weights are given by

$$\gamma_0 = \gamma_{Hi}; \qquad \gamma_1 = (1-\gamma_{Hi})\gamma_{Lo}; \qquad \gamma_2 = \gamma_3 = \gamma_4 = (1-\gamma_{Hi})(1-\gamma_{Lo})/3 \tag{3.18}$$

Notice that the third order central stencil should carry a higher linear weight than the other three one-sided third order stencils because this helps to make the third order WENO centrally biased on the unstructured mesh. Also notice that $\gamma_1+\gamma_2+\gamma_3+\gamma_4 = 1-\gamma_{Hi}$. Typically, we set $\gamma_{Hi} \in [0.75, 0.95]$ and $\gamma_{Lo} \in [0.75, 0.95]$. These numbers themselves give us a glimpse of what is afoot. When a suitable comparison of the smoothness indicators shows that the large fifth order central stencil is smooth we want most (or all) of our reconstruction to come from the large central stencil. However, when a suitable comparison of the smoothness indicators shows that the large central stencil is non-smooth, we want most (or all) of our reconstruction to be weighted towards our very stable, third order accurate, extrema-preserving WENO reconstruction from Section 2. In the next paragraph we describe the construction of the non-linear weights. In the paragraph after that, we describe the assembly of the non-linearly hybridized higher order reconstruction.

We now describe the process of obtaining the non-linear weights for WENO-AO(5,3) reconstruction. To avoid loss of order at inflection points we use the smoothness indicators to define

$$\tau = \frac{1}{4}\big(|\beta_0-\beta_1| + |\beta_0-\beta_2| + |\beta_0-\beta_3| + |\beta_0-\beta_4|\big) \tag{3.19}$$

Recall that β_0 was defined in eqn. (3.17) whereas β_1 through β_4 were documented in the narrative that follows eqn. (2.16). Using the smoothness indicators again, and following Borges et al. [22], we can obtain the un-normalized weights using the WENO-Z option as

$$w_i = \gamma_i\big(1+\tau^2/(\beta_i+\varepsilon)^2\big) \quad \text{for } i = 0,\ldots,4 \tag{3.20a}$$

If the solution is not dominated by inflection points, it may even be acceptable to use the original WENO strategy for obtaining the un-normalized weights given by

$$w_i = \gamma_i/(\beta_i+\varepsilon)^p \quad \text{for } i = 0,\ldots,4 \tag{3.20b}$$

Here $p=2$ or $p=4$ are traditionally used; and ε is a very tiny number, typically $\varepsilon \sim 10^{-12}$. We have found eqn. (3.20b) to be a more stable option while eqn. (3.20a) is a more accurate option. In practice, we have used eqn. (3.20a) in this paper. The normalized weights are given by

$$\bar{w}_i = w_i \Big/ \left(\sum_{k=0}^{4} w_k\right) \quad \text{for } i = 0,\ldots,4 \tag{3.21}$$

In principle, the WENO-Z option from eqn. (3.20a) is slightly better at inflection points, but the other choice from eqn. (3.20b) is also very popular. So we have documented both options. This completes the description of the normalized, non-linear weights for WENO-AO(5,3). The same strategy also works for WENO-AO(4,3).

Say we denote the reconstructed polynomial from WENO-AO(5,3) as $R^{AO(5,3)}(x,y)$. Our task in this paragraph is to describe the construction of the order-preserving, non-linearly hybridized, fifth order polynomial $R^{AO(5,3)}(x,y)$. The non-linear weights should be combined in such a way that when all the smoothness indicators seem to have almost similar values then only the higher order scheme is obtained. Such a combination strategy was demonstrated in Balsara, Garain and Shu [14] for non-linearly hybridizing a fifth order polynomial with three quadratic polynomials for structured meshes. A similar idea can be used to make a non-linear hybridization between the fifth order polynomial associated with the central stencil from Sub-section 3.2 and the four third order polynomials from Section 2. The latter four stencils are associated with the

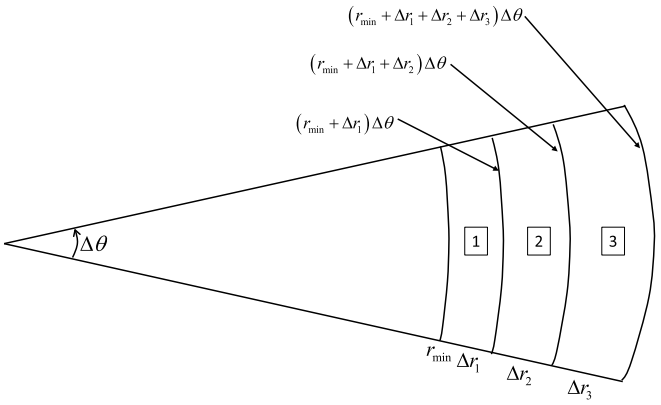

Fig. 3. Shows three successive zones in the radial direction. It also shows their radial extent as well as the arc length associated with each of them. The ratio of the arc length to the radial extent for each zone should remain the same if the zones are all to be similar to one another. When such a similarity prevails, the reconstruction matrices from one radial zone to the next will be identical.

third order WENO reconstruction described in eqn. (2.19). Realize, therefore, that when the five smoothness measures associated with these five stencils have closely similar values, we have $\bar{w}_i \to \gamma_i$ for $i = 1, \ldots, 3$. We then require that when the limits specified by the previous sentence are attained, we have $R^{\mathrm{AO}(5,3)}(x, y) \to R^{p4;0}(x, y)$. This is achieved by the following definition

$$R^{\mathrm{AO}(5,3)}(x, y) = \frac{\bar{w}_0}{\gamma_0}\left(R^{p4;0}(x, y) - \left(\sum_{k=1}^{4} \gamma_k R^{p2;k}(x, y)\right)\right) + \left(\sum_{k=1}^{4} \bar{w}_k R^{p2;k}(x, y)\right) \tag{3.22}$$

Notice that in the limit where the smoothness indicators for all the stencils have closely similar values, we do have $R^{\mathrm{AO}(5,3)}(x, y) \to R^{p4;0}(x, y)$. In the limit where the larger stencil has a very non-smooth solution, we have $\bar{w}_0 \ll \bar{w}_i$ for $i = 1, \ldots, 4$. This ensures that the smoothest of the third order WENO stencils will be sought out by the reconstruction polynomial. Notice that the non-linear hybridization that we sought at the beginning of this paragraph has been found via eqn. (3.22).

The interested reader may always ask why we choose the WENO with second degree polynomial stencils as being effectively the fully stable one? It is always possible to claim that for problems involving interacting shocks, all the stencils with second degree polynomials might contain shocks. In such a situation, a purist might always insist that one should drop down to smaller stencils with perhaps linear polynomials. It is worth pointing out that practical experience on structured and unstructured meshes (Balsara, Garain and Shu [14], Dumbser and Käser [34]) has shown that with appropriate non-linear hybridization the stencils with second degree polynomials perform very well even in the vicinity of interacting shocks. Please see Fig. 5 from Balsara, Garain and Shu [14], which illustrates this point for a problem with interacting strong shocks.

4. Simplification of the algorithm on spherical (or self-similar) meshes

For spherical meshes (or for cylindrical meshes) a particularly efficient WENO strategy presents itself. The strategy is so efficient that it allows an entire row of zones on in the mesh to be processed by making only one inversion of the least squares matrix for each stencil. For all such spherical meshes, whether they use logically Cartesian (r, θ, ϕ) coordinates, or whether they use some geodesic-based tessellation of the sphere, there is a strong desire to concentrate zones in a ratioed fashion at the boundary of the sphere. In all such circumstances, as long as the mesh ratioing is done in a geometric fashion, it is possible to utilize self-similarity to dramatically simplify the calculation. This is shown in the next paragraph.

Consider Fig. 3 which shows zones in the radial direction starting from a radius of $r_{\min}$. The top of the first zone has radius $r_1 = r_{\min} + \Delta r_1$ and an arc length of $r_1\Delta\theta$. The top of the second zone in Fig. 3 has a radius $r_2 = r_1 + \Delta r_2$ and an arc length of $r_2\Delta\theta$. The top of the third zone in Fig. 3 has a radius $r_3 = r_2 + \Delta r_2$ and an arc length of $r_3\Delta\theta$; and so on. To have true self-similarity, we want any target zone (and the halo of zones around it) to look like any other target zone (and the halo around this other target zone). This happens if all the zones have the same aspect ratio. When such a similarity prevails, the reconstruction matrices from one radial zone to the next will be identical. In other words, we want

$$\frac{r_1\Delta\theta}{\Delta r_1} = \frac{r_2\Delta\theta}{\Delta r_2} = \frac{r_3\Delta\theta}{\Delta r_3} = \ldots \tag{4.1}$$

Eliminating $\Delta\theta$ in the above equation, and using componendo-dividendo rules, we get

$$\frac{r_1}{r_2} = \frac{r_2}{r_3} = \frac{r_3}{r_4} = \ldots \tag{4.2}$$

In other words, the radius of each zone boundary is the geometric mean of the two zone boundaries on either side of it. Simply put, we have

$$r_j = \sqrt{r_{j-1} r_{j+1}} \tag{4.3}$$

If the above equation is satisfied, all zones in the same radial direction will be self-similar to the first zone being considered. As a result, one only needs to invert and store the least squares matrices for the stencils in that first zone. The inverted least squares matrices can then be reused for WENO reconstruction in all the other zones in that radial direction. This produces an enormous simplification in storage and processing of meshes in spherical (and cylindrical) geometries.

5. A pointwise description of implementation-related details

We describe a pointwise procedure for implementing the WENO-AO algorithm. The first four points below should only be done once at the time of initialization. The entire WENO-AO algorithm is described in the following steps:

1) Find the centroid of each zone. This is the unique point within each zone about which the first moments vanish. The centroid can even be found by using numerical quadrature, as long as the numerical quadrature is of sufficiently high order of accuracy, i.e. at least as high order as the accuracy of the desired scheme. In this work, we used quadrature that was at least one order of accuracy higher than that of the WENO scheme. This point needs to be done globally once at the beginning of the code for static meshes. In case we have mesh motion, as is common in any form of ALE-type scheme, this point needs to be repeated (globally) after mesh motion. If any form of local adaptation is used, this step has to be repeated in the locally adapted zones.

2) Using the radius of an in-circle, or circumcircle for each element, obtain a characteristic length for each element.

3) For each zone, we evaluate the geometric moments. For third order, use eqns. (2.4) and (2.7) to evaluate the geometric moments. This will enable us to expand the reconstructed polynomial for any stencil in terms of the basis set given in eqn. (2.6). For fourth order, use eqns. (3.2) and (3.4) to evaluate the geometric moments. This enables us to expand the reconstructed polynomial for the fourth order central stencil in terms of the basis set given in eqn. (3.3). Sub-section 3.2 provides much of the additional detail for fifth order reconstruction. (Appendix A gives details for the three-dimensional version of the algorithm discussed here.)

4) For each two-dimensional triangular zone, identify the central stencil and the three one-sided stencils, as shown in Fig. 1 and the associated discussion. For three-dimensional tetrahedral meshes, there will be a central stencil and four one-sided stencils. If a higher order WENO scheme is to be built, choose a suitably larger central stencil. Identification of a stencil is tantamount to having a list of zones that participate in a given stencil.

5) For each of the four third order stencils in two-dimensions, visit each of the elements in that stencil. The target element, i.e. the zone on which the reconstruction is being carried out, should be excluded. For each element in the stencil, eqn. (2.15) provides one row of the least squares system for that chosen stencil. Assemble that least squares matrix and the right hand side. Minimize the least squares system for each stencil to obtain the modes of the third order polynomial shown in eqn. (2.6). In three-dimensions, an analogue of eqn. (2.15) is easily built. If a large fourth order stencil is also present, eqn. (3.9) provides one row of the squares system for that fourth order stencil. Least squares minimization of that system will provide the modes of the fourth order polynomial shown in eqn. (3.3). If a fifth order stencil is present, obtain the analogous extension of eqn. (3.9). Least squares minimization of that system will provide the modes of the fifth order polynomial shown in eqn. (3.11). The three-dimensional extension of eqn. (3.9) is also easily obtained. For each stencil that is not close to the physical boundary, we have by now obtained all the modes of the polynomial basis expansion.

6) If a third order scheme is desired, construct smoothness indicators as in eqn. (2.16); make normalized non-linear weights as in eqn. (2.17) and (2.18); then use eqn. (2.19) to obtain a third order accurate WENO reconstruction for unstructured meshes. This procedure transparently extends to three-dimensions.

7) If a fourth or higher order scheme is desired, construct the smoothness indicators for the higher order stencils as in eqn. (3.17). Use eqns. (3.18) to (3.21) to make the normalized non-linear weights. Then use eqn. (3.22), or its higher order analogue, to obtain a fourth or higher order accurate WENO reconstruction for unstructured meshes. This procedure also transparently extends to three-dimensions.

There is a more efficient variant of this algorithm that trades memory for efficiency. In other words, if ample amounts of computer memory are available, then a faster algorithm becomes possible. This variant will work at least in the limit when the mesh is not moving. The simplification consists of realizing that the least squares matrix in step 5 above only needs to be constructed once for each stencil and stored in the computer's memory. The corresponding matrix system only consists of geometrical terms and can be inverted once and for all during the initialization step. In that situation, step 5 above only requires the evaluation of a right hand side and its matrix multiplication with the pre-computed inverted matrix for any given stencil. As shown in Section 4, when self-similarity can be exploited, the matrix assembly and storage becomes even simpler.

For applications that do not use ALE methods, the previous paragraph provides the fastest implementation. For ALE methods, where the mesh geometry keeps changing, or when computer memory is at a premium, one may need to use

step 5 and resort to a matrix inversion for each time step. Even in such circumstances, if the conservation law has a large number of components, the least squares matrix assembly and inversion only needs to be done once per stencil and need not be repeated when reconstructing each of the components of the conservation law.

6. Results – order of accuracy in multiple space dimensions

To illustrate the versatility of our WENO-AO algorithms, we show results from two families of codes. The first code is three dimensional and it maps the sphere as perfectly as possible, as described below. The second code is a regular unstructured mesh code that can function without mesh motion as well as have ALE-type capabilities. For each sub-section we identify the kind of mesh used for that test problem.

The first code uses a geodesic mesh on a sphere which has been extruded out in the radial direction. Starting from a spherical icosahedron, the spherical triangles are successively bisected. As a result, the surface of the sphere is triangulated as perfectly as possible with great triangles that are (for the most part) as close as possible to equilateral triangles. This meshing gives us the most isotropic Delaunay triangulated meshing of the sphere that is possible. The extrusion in the radial direction ensures that each element of the mesh is a frustrum which can be mapped to a triangular prism. Isoparametric mapping that is linear, quadratic and cubic is used to map the reference triangular prism to the spherical frustrum formed by each element. When a cubic isoparametric mapping is used, the mapping is fourth order accurate, as is the fourth order scheme that we implemented. Therefore, the linear and quadratic mappings can be thought of as sub-parametric, while the cubic mapping is fully isoparametric. Up to fourth order accurate spatial reconstruction from WENO-AO was implemented on this spherical mesh. At fourth order, we used a central stencil along with six forward sector stencils for all our three-dimensional simulations on the geodesic mesh. The forward sector stencils were upwind biased towards the six vertices of the frustrum. We also used $\gamma_{Hi} = \gamma_{Lo} = 0.95$ in eqns. (3.18). At second and third order, we used seven (somewhat smaller) stencils with a similar philosophy but with $\gamma_C = 50$ in eqn. (2.17). All geodesic mesh calculations achieved non-linear hybridization by using eqn. (3.20b). This spatial reconstruction was coupled to an SSP-RK scheme with temporal accuracy that matches the spatial accuracy (Shu and Osher [60,61], Spiteri and Ruuth [64,65]). In keeping with the ideas on isoparametric mapping, the curvature of the spherical faces was included in the quadrature formulae for the flux evaluation and the quadrature in the annular faces of each zone was also treated precisely. Algorithmic details for the geodesic mesh are provided in Balsara et al. [20]. Notice that the mesh used is ratioed in the radial direction. As a result, each zone of this mesh is topologically similar to a triangular prism; see Fig. 2 of that paper. But, because of the ratioing in the radial direction, each prism is much narrower at the inner radius and broader at the outer radius. This affects the CFL because the smallest side of each zone has to be used when computing the CFL. For this reason, the CFLs of such codes are a little smaller than the traditional CFL because one side of the zone is much narrower than the other side of the zone.

The second code uses a regular unstructured mesh which can be used with or without ALE-type mesh motion. The WENO-AO provides the spatial reconstruction. Up to fifth order accurate reconstruction was included in the code. The ADER method (Dumbser et al. [35]) was used for the temporal evolution resulting in a single step update where the reconstruction was done only once per timestep. When the ALE capabilities of the code were used, mesh motion was provided by using multidimensional Riemann solvers (Balsara, [9,10,12], Boscheri et al. [23,24], Balsara and Nkonga [15]). For a detailed description of the ADER-ALE algorithm the reader is referred to (Boscheri et al. [25–27]). Regardless of order, the two-dimensional ALE code with WENO-AO used one large central stencil, one smaller central stencil and three forward sector stencils (see Fig. 1) with $\gamma_{Hi} = \gamma_{Lo} = 0.95$ in eqns. (3.18). All unstructured mesh calculations achieved non-linear hybridization by using eqn. (3.20a). The mesh used in this second code is a traditional unstructured mesh and there is no problem with using CFLs that are as large as 0.5 in all the reported simulations from this code.

6.1. Spherical geodesic mesh: solar wind on spherical meshes

A stellar wind is a continuous supersonic outflow of ionized gases from the atmosphere of a star. One of the simplest models for the stellar wind is a spherically symmetric (all variables depend on radial distance R measured from the center of the star) expansion of a polytropic gas into space (Parker, [77]). In a weakly magnetized case the flow is given by the solution of

$$\frac{\tilde{v}^2 - 1}{2} + \frac{\tilde{R}^{2(1-\gamma)}\tilde{v}^{(1-\gamma)} - 1}{\gamma - 1} - 2\left(\frac{1}{\tilde{R}} - 1\right) = 0, \tag{6.1}$$

$$\tilde{\rho} = \frac{1}{\tilde{v}\tilde{R}^2},$$

$$\tilde{P} = \tilde{\rho}^{\gamma}.$$

Quantities with the tilde on top denote the radial distance, density, radial velocity, and pressure normalized to their values at the critical point $R = R_c$, where the flow velocity equals the sound speed. At large distances from the star (well beyond the critical point) the force of gravity may be neglected and equation (6.1) becomes

Table 1a
The table shows the accuracy analysis for the second-order WENO scheme for the solar wind on spherical meshes. A CFL of 0.25 was used. The errors and accuracy in the density (ρ) and x-momentum (m_x) are shown.

Angular size (in degrees)	ρ L_1 error	ρ L_1 accuracy	ρ $L_{\inf}$ error	ρ $L_{\inf}$ accuracy
7.925	8.6233E−05		1.6185E−04	
3.962	2.0239E−05	2.09	4.3210E−05	1.91
1.981	5.2455E−06	1.95	1.4638E−05	1.56
0.991	1.3577E−06	1.95	6.3307E−06	1.21
Angular size (in degrees)	m_x L_1 error	m_x L_1 accuracy	m_x $L_{\inf}$ error	m_x $L_{\inf}$ accuracy
7.925	2.0841E−04		4.2383E−04	
3.962	5.1914E−05	2.01	1.1087E−04	1.93
1.981	1.3205E−05	1.98	3.8251E−05	1.54
0.991	3.3509E−06	1.98	1.5359E−05	1.32

Table 1b
The table shows the accuracy analysis for the third-order WENO scheme for the solar wind on spherical meshes. A CFL of 0.25 was used. The errors and accuracy in the density (ρ) and x-momentum (m_x) are shown.

Angular size (in degrees)	ρ L_1 error	ρ L_1 accuracy	ρ $L_{\inf}$ error	ρ $L_{\inf}$ accuracy
7.925	4.1558E−05		7.8614E−05	
3.962	5.6337E−06	2.88	1.1236E−05	2.81
1.981	7.2899E−07	2.95	1.4637E−06	2.94
0.991	9.2576E−08	2.98	1.9935E−07	2.88
Angular size (in degrees)	m_x L_1 error	m_x L_1 accuracy	m_x $L_{\inf}$ error	m_x $L_{\inf}$ accuracy
7.925	6.7677E−05		1.5859E−04	
3.962	8.0631E−06	3.07	1.8145E−05	3.13
1.981	1.0051E−06	3.00	2.1916E−06	3.05
0.991	1.2675E−07	2.99	4.0494E−07	2.44

Table 1c
The table shows the accuracy analysis for the fourth-order WENO scheme for the solar wind on spherical meshes. A CFL of 0.25 was used. The errors and accuracy in the density (ρ) and x-momentum (m_x) are shown.

Angular size (in degrees)	ρ L_1 error	ρ L_1 accuracy	ρ $L_{\inf}$ error	ρ $L_{\inf}$ accuracy
7.925	1.0069E−05		2.0471E−05	
3.962	4.6732E−07	4.43	1.7192E−06	3.57
1.981	2.9786E−08	3.97	2.2732E−07	2.92
0.991	2.1204E−09	3.81	2.6227E−08	3.12
Angular size (in degrees)	m_x L_1 error	m_x L_1 accuracy	m_x $L_{\inf}$ error	m_x $L_{\inf}$ accuracy
7.925	2.4760E−05		5.1096E−05	
3.962	9.9519E−07	4.64	4.2656E−06	3.58
1.981	5.1718E−08	4.27	5.4669E−07	2.96
0.991	3.3236E−09	3.96	6.2537E−08	3.13

$$\frac{\tilde{v}^2-1}{2}+\frac{\tilde{R}^{2(1-\gamma)}\tilde{v}^{(1-\gamma)}-1}{M_0^2(\gamma-1)}=0. \tag{6.2}$$

In eqn (6.2) the tilde quantities are normalized to some reference radius where the flow is already supersonic with a Mach number $M_0 > 1$. The simulation was initialized with a solution to (6.2) obtained using Newton's method on a domain of radial extent [2:3.5]. We used $\gamma = 1.4$, the reference radius of one and the values of density, velocity and pressure all equal to unity at that distance, which yields $M_0 = \sqrt{\gamma} \approx 1.2$. This problem was run till a time of 0.25.

The second order WENO scheme uses simple, piecewise-linear interpolation and is included for completeness. The third order WENO scheme is based on the method described in Section 2. The WENO-AO(4,3) scheme is based on the algorithm described in Section 3.1. Tables 1a, 1b and 1c show the accuracy analysis for second, third and fourth order simulations, respectively. For the time integration, we used SSP-RK schemes with temporal order that matches the spatial order of accuracy. The results are shown for the situation where second order isoparametric mapping is used to map the triangular prisms

Table 2a
The table shows the accuracy analysis for the second-order WENO scheme for the method of manufactured solution on spherical meshes. A CFL of 0.25 was used. The errors and accuracy in the density (ρ) and x-momentum (m_x) are shown.

Angular size (in degrees)	ρ L_1 error	ρ L_1 accuracy	ρ L_{inf} error	ρ L_{inf} accuracy
7.925	1.5631E−04		2.8996E−04	
3.962	3.5544E−05	2.14	7.7206E−05	1.91
1.981	8.7083E−06	2.03	1.9920E−05	1.95
0.991	2.1688E−06	2.01	5.0472E−06	1.98
Angular size (in degrees)	m_x L_1 error	m_x L_1 accuracy	m_x L_{inf} error	m_x L_{inf} accuracy
7.925	2.1010E−04		4.2611E−04	
3.962	5.1761E−05	2.02	1.1192E−04	1.93
1.981	1.2874E−05	2.01	2.8658E−05	1.97
0.991	3.2169E−06	2.00	9.8811E−06	1.54

Table 2b
The table shows the accuracy analysis for the third-order WENO scheme for the method of manufactured solution on spherical meshes. A CFL of 0.25 was used. The errors and accuracy in the density (ρ) and x-momentum (m_x) are shown.

Angular size (in degrees)	ρ L_1 error	ρ L_1 accuracy	ρ L_{inf} error	ρ L_{inf} accuracy
7.925	7.5177E−05		1.3145E−04	
3.962	1.0268E−05	2.87	1.8422E−05	2.83
1.981	1.3137E−06	2.97	2.3806E−06	2.95
0.991	1.6527E−07	2.99	3.2278E−07	2.88
Angular size (in degrees)	m_x L_1 error	m_x L_1 accuracy	m_x L_{inf} error	m_x L_{inf} accuracy
7.925	6.8752E−05		1.6133E−04	
3.962	8.1940E−06	3.07	1.8180E−05	3.15
1.981	1.0123E−06	3.02	2.1982E−06	3.05
0.991	1.2705E−07	2.99	2.9499E−07	2.90

to spherical frustrums. On the coarsest level, the spherical mesh has the angular resolution of 5.625° and 8 logarithmically binned radial zones. On the finest level, the spherical mesh has the angular resolution of 0.703° and 64 logarithmically binned radial zones. We can see that the schemes achieve their design accuracies.

6.2. Spherical geodesic mesh: method of manufactured solution on spherical meshes

This test problem has been adopted from Ivan et al. [78] and suitably modified for a purely hydrodynamical simulation. In this problem, the exact solution is given by the vector of primitive variables as $(\rho, P, v_x, v_y, v_z) = (R^{-\frac{5}{2}}, R^{-\frac{5}{2}}, \frac{x}{\sqrt{R}}, \frac{y}{\sqrt{R}}, \frac{z}{\sqrt{R}} + \kappa R^{\frac{5}{2}})$. This exact solution is obtained from the Euler equations with the source term given by

$$\begin{bmatrix} 0, \\ \frac{1}{2}R^{-2} + \kappa z(3.5R^{-1} + 2\kappa z) + \frac{(\kappa R)^2}{2}(5\kappa z R + 7), \\ \frac{1}{2}xR^{-\frac{5}{2}}(R^{-1} - 5R^{-2} - \kappa z), \\ \frac{1}{2}yR^{-\frac{5}{2}}(R^{-1} - 5R^{-2} - \kappa z), \\ \frac{1}{2}zR^{-\frac{5}{2}}(R^{-1} - 5R^{-2} - \kappa z) + \frac{5}{2}\kappa R^{-\frac{1}{2}}(1 + \kappa z R) + \kappa R^{-\frac{1}{2}} \end{bmatrix}.$$

Here, $R = \sqrt{x^2 + y^2 + z^2}$ and as suggested in Ivan et al. [78], we use $\kappa = 0.017$. This problem is initialized inside a spherical domain with radial extent $[2 : 3.5]$. We used a three-dimensional geodesic mesh with zones that form spherical triangles when projected on to the unit sphere. In the ghost zones of the upper and lower radial boundary, we provide the zone averaged values of the exact solution. These zone averaged values are evaluated using high-order accurate quadrature points. For this problem, we used a stopping time of 0.25 and $\gamma = 7/5$.

The second order WENO scheme uses simple, piecewise-linear interpolation and is included for completeness. The third order WENO scheme is based on the method described in Section 2. The WENO-AO(4,3) scheme is based on the algorithm described in Section 3.1. Tables 2a, 2b and 2c show the accuracy analysis for second, third and fourth order runs, respectively. For the time integration, we used SSP-RK schemes with temporal order that matches the spatial order of accuracy. The results are shown for the situation where third order isoparametric mapping is used to map the triangular prisms to spherical frustrums. On the coarsest level, the spherical mesh has the angular resolution of 5.625° and 8 logarithmically

Table 2c
The table shows the accuracy analysis for the fourth-order WENO scheme for the method of manufactured solution on spherical meshes. A CFL of 0.25 was used. The errors and accuracy in the density (ρ) and x-momentum (m_x) are shown.

Angular size (in degrees)	ρ L_1 error	ρ L_1 accuracy	ρ $L_{\inf}$ error	ρ $L_{\inf}$ accuracy
7.925	1.8430E−05		3.6866E−05	
3.962	8.1022E−07	4.51	1.9642E−06	4.23
1.981	4.2407E−08	4.26	1.8713E−07	3.39
0.991	2.5237E−09	4.07	2.2846E−08	3.03
Angular size (in degrees)	m_x L_1 error	m_x L_1 accuracy	m_x $L_{\inf}$ error	m_x $L_{\inf}$ accuracy
7.925	2.5092E−05		5.1456E−05	
3.962	9.9576E−07	4.66	2.8303E−06	4.18
1.981	4.6000E−08	4.44	3.2183E−07	3.14
0.991	2.5904E−09	4.15	3.9207E−08	3.04

Table 3a
The table shows the accuracy analysis for the second-order WENO scheme for the method of manufactured solution on spherical meshes. A CFL of 0.25 was used. The errors and accuracy in the density (ρ) and x-momentum (m_x) are shown.

Angular size (in degrees)	ρ L_1 error	ρ L_1 accuracy	ρ $L_{\inf}$ error	ρ $L_{\inf}$ accuracy
7.925	1.8156E−04		3.2563E−04	
3.962	3.6534E−05	2.31	7.5258E−05	2.11
1.981	8.5767E−06	2.09	1.9467E−05	1.95
0.991	2.1168E−06	2.02	5.1555E−06	1.92
Angular size (in degrees)	m_x L_1 error	m_x L_1 accuracy	m_x $L_{\inf}$ error	m_x $L_{\inf}$ accuracy
7.925	2.1267E−04		4.2943E−04	
3.962	5.1546E−05	2.04	1.1015E−04	1.96
1.981	1.2757E−05	2.01	2.8227E−05	1.96
0.991	3.1824E−06	2.00	1.0597E−05	1.41

Table 3b
The table shows the accuracy analysis for the third-order WENO scheme for the method of manufactured solution on spherical meshes. A CFL of 0.25 was used. The errors and accuracy in the density (ρ) and x-momentum (m_x) are shown.

Angular size (in degrees)	ρ L_1 error	ρ L_1 accuracy	ρ $L_{\inf}$ error	ρ $L_{\inf}$ accuracy
7.925	5.4496E−05		9.5615E−05	
3.962	7.8704E−06	2.79	1.4496E−05	2.72
1.981	1.0169E−06	2.95	1.9490E−06	2.89
0.991	1.2784E−07	2.99	2.5167E−07	2.95
Angular size (in degrees)	m_x L_1 error	m_x L_1 accuracy	m_x $L_{\inf}$ error	m_x $L_{\inf}$ accuracy
7.925	4.9159E−05		1.2456E−04	
3.962	5.1857E−06	3.24	1.1195E−05	3.48
1.981	6.1178E−07	3.08	1.4484E−06	2.95
0.991	7.5421E−08	3.02	1.8330E−07	2.98

binned radial zones. On the finest level, the spherical mesh has the angular resolution of 0.703° and 64 logarithmically binned radial zones. We can see that the schemes achieve their design accuracies.

In Section 3 we mentioned that we use $\gamma_{Hi} \in [0.75, 0.95]$ and $\gamma_{Lo} \in [0.75, 0.95]$. However, the results in Tables 1 and 2 were obtained with $\gamma_{Hi} = 0.85$ and $\gamma_{Lo} = 0.85$. It is desirable to show that our WENO-AO scheme is quite insensitive to the specific values of γ_{Hi} and γ_{Lo}. Recall that γ_{Lo} can be used for second and third order schemes too. To show that the order property is insensitive to variations in γ_{Hi} and γ_{Lo}, we present Table 3 with $\gamma_{Hi} = 0.75$ and $\gamma_{Lo} = 0.75$. We also present Table 4 which uses $\gamma_{Hi} = 0.95$ and $\gamma_{Lo} = 0.95$. We see from Tables 3a, 3b, 3c and 4a, 4b, 4c that the order property is indeed unchanged. This shows that our WENO-AO scheme is quite insensitive to the specific values of the coefficients that are used.

Table 3c
The table shows the accuracy analysis for the fourth-order WENO scheme for the method of manufactured solution on spherical meshes. A CFL of 0.25 was used. The errors and accuracy in the density (ρ) and x-momentum (m_x) are shown.

Angular size (in degrees)	ρ L_1 error	ρ L_1 accuracy	ρ L_{inf} error	ρ L_{inf} accuracy
7.925	1.8420E−05		3.6829E−05	
3.962	8.1129E−07	4.50	1.9647E−06	4.23
1.981	4.2445E−08	4.26	1.8797E−07	3.39
0.991	2.5237E−09	4.07	2.3265E−08	3.01
Angular size (in degrees)	m_x L_1 error	m_x L_1 accuracy	m_x L_{inf} error	m_x L_{inf} accuracy
7.925	2.5077E−05		5.1454E−05	
3.962	9.9689E−07	4.65	2.8346E−06	4.18
1.981	4.6044E−08	4.44	3.2337E−07	3.13
0.991	2.5904E−09	4.15	3.9657E−08	3.03

Table 4a
The table shows the accuracy analysis for the second-order WENO scheme for the method of manufactured solution on spherical meshes. A CFL of 0.25 was used. The errors and accuracy in the density (ρ) and x-momentum (m_x) are shown.

Angular size (in degrees)	ρ L_1 error	ρ L_1 accuracy	ρ L_{inf} error	ρ L_{inf} accuracy
7.925	1.4425E−04		2.9570E−04	
3.962	3.5749E−05	2.01	7.9194E−05	1.90
1.981	8.9123E−06	2.00	2.0373E−05	1.96
0.991	2.2277E−06	2.00	5.1584E−06	1.98
Angular size (in degrees)	m_x L_1 error	m_x L_1 accuracy	m_x L_{inf} error	m_x L_{inf} accuracy
7.925	2.0958E−04		4.3064E−04	
3.962	5.2234E−05	2.00	1.1369E−04	1.92
1.981	1.3044E−05	2.00	2.9091E−05	1.97
0.991	3.2645E−06	2.00	9.1867E−06	1.66

Table 4b
The table shows the accuracy analysis for the third-order WENO scheme for the method of manufactured solution on spherical meshes. A CFL of 0.25 was used. The errors and accuracy in the density (ρ) and x-momentum (m_x) are shown.

Angular size (in degrees)	ρ L_1 error	ρ L_1 accuracy	ρ L_{inf} error	ρ L_{inf} accuracy
7.925	9.7628E−05		1.7027E−04	
3.962	1.2731E−05	2.94	2.2914E−05	2.89
1.981	1.6145E−06	2.98	2.9211E−06	2.97
0.991	2.0283E−07	2.99	4.1588E−07	2.81
Angular size (in degrees)	m_x L_1 error	m_x L_1 accuracy	m_x L_{inf} error	m_x L_{inf} accuracy
7.925	8.9188E−05		1.9430E−04	
3.962	1.1386E−05	2.97	2.5608E−05	2.92
1.981	1.4423E−06	2.98	3.2673E−06	2.97
0.991	1.8254E−07	2.98	4.3948E−07	2.89

6.3. Unstructured mesh without and with ale: isentropic hydrodynamical vortex

To demonstrate the multidimensional accuracy of our WENO-AO schemes on unstructured meshes, we use the isentropic fluid vortex test from Jiang and Shu [47]. The problem is initialized on a two-dimensional unstructured mesh that spans $[-5, 15] \times [-5, 5]$. Traditionally, on a structured mesh, the vortex would be made to propagate along the diagonal of the mesh. However, for an unstructured mesh, this is irrelevant, and we cause the vortex to propagate in the x-direction over a distance of 10 units. An unperturbed flow for the Euler equations is chosen with $(\rho, P, v_x, v_y) = (1, 1, 0, 1)$ and with ratio of specific heats $\gamma = 1.4$ is initialized on the unstructured mesh. The temperature and entropy are defined by $T = P/\rho$ and $S = P/\rho^{\gamma}$. The vortex is defined as a fluctuation to this mean flow given by

$$(\delta v_x, \delta v_y) = \frac{\varepsilon}{2\pi} e^{0.5(1-r^2)}(-y, x)$$

Table 4c
The table shows the accuracy analysis for the fourth-order WENO scheme for the method of manufactured solution on spherical meshes. A CFL of 0.25 was used. The errors and accuracy in the density (ρ) and x-momentum (m_x) are shown.

Angular size (in degrees)	ρ L_1 error	ρ L_1 accuracy	ρ $L_{\inf}$ error	ρ $L_{\inf}$ accuracy
7.925	1.8420E−05		3.6829E−05	
3.962	8.1129E−07	4.50	1.9647E−06	4.23
1.981	4.2445E−08	4.26	1.8797E−07	3.39
0.991	2.5237E−09	4.07	2.3265E−08	3.01
Angular size (in degrees)	m_x L_1 error	m_x L_1 accuracy	m_x $L_{\inf}$ error	m_x $L_{\inf}$ accuracy
7.925	2.5077E−05		5.1457E−05	
3.962	9.9689E−07	4.65	2.8346E−06	4.18
1.981	4.6044E−08	4.44	3.2337E−07	3.13
0.991	2.5904E−09	4.15	3.9657E−08	3.03

Table 5
The table shows the accuracy analysis for the hydrodynamical vortex problem as measured in the density variable.

Method	Element size, h	L_1 error	L_1 order	L_∞ error	L_∞ order
WENO 3rd Order Eulerian (fixed mesh)	$3.2476 \cdot 10^{-1}$	$7.9950 \cdot 10^{-2}$	–	$2.0007 \cdot 10^{-2}$	–
	$2.4837 \cdot 10^{-1}$	$3.9448 \cdot 10^{-2}$	**2.6**	$9.0074 \cdot 10^{-3}$	**3.0**
	$1.6336 \cdot 10^{-1}$	$1.3362 \cdot 10^{-2}$	**2.6**	$2.8225 \cdot 10^{-3}$	**2.8**
	$1.2811 \cdot 10^{-1}$	$5.8711 \cdot 10^{-3}$	**3.4**	$1.3839 \cdot 10^{-3}$	**2.9**
WENO 3rd Order ALE (moving mesh)	$3.2936 \cdot 10^{-1}$	$6.0638 \cdot 10^{-2}$	–	$1.3994 \cdot 10^{-2}$	–
	$2.5118 \cdot 10^{-1}$	$2.6351 \cdot 10^{-2}$	**3.1**	$5.3706 \cdot 10^{-3}$	**3.5**
	$1.6757 \cdot 10^{-1}$	$8.5445 \cdot 10^{-3}$	**2.8**	$1.9207 \cdot 10^{-3}$	**2.5**
	$1.2781 \cdot 10^{-1}$	$3.4613 \cdot 10^{-3}$	**3.3**	$8.4560 \cdot 10^{-4}$	**3.0**
WENO-AO(4,3) Eulerian (fixed mesh)	$3.2476 \cdot 10^{-1}$	$2.4369 \cdot 10^{-2}$	–	$7.0007 \cdot 10^{-3}$	
	$2.4837 \cdot 10^{-1}$	$8.0741 \cdot 10^{-3}$	**4.1**	$1.8866 \cdot 10^{-3}$	**4.9**
	$1.6336 \cdot 10^{-1}$	$1.4910 \cdot 10^{-3}$	**4.0**	$4.0097 \cdot 10^{-4}$	**3.7**
	$1.2811 \cdot 10^{-1}$	$5.0134 \cdot 10^{-4}$	**4.5**	$2.2025 \cdot 10^{-4}$	**2.5**
WENO-AO(4,3) ALE (moving mesh)	$3.2873 \cdot 10^{-1}$	$1.8373 \cdot 10^{-2}$	–	$4.0138 \cdot 10^{-3}$	
	$2.5098 \cdot 10^{-1}$	$6.6598 \cdot 10^{-3}$	**3.8**	$1.5404 \cdot 10^{-3}$	**3.5**
	$1.6752 \cdot 10^{-1}$	$1.5044 \cdot 10^{-3}$	**3.7**	$4.1024 \cdot 10^{-4}$	**3.3**
	$1.2777 \cdot 10^{-1}$	$4.6699 \cdot 10^{-4}$	**4.3**	$1.4565 \cdot 10^{-4}$	**3.8**
WENO-AO(5,3) Eulerian (fixed mesh)	$3.2476 \cdot 10^{-1}$	$3.5950 \cdot 10^{-2}$	–	$9.6827 \cdot 10^{-3}$	
	$2.4837 \cdot 10^{-1}$	$9.5362 \cdot 10^{-3}$	**4.9**	$2.1702 \cdot 10^{-3}$	**5.6**
	$1.6336 \cdot 10^{-1}$	$1.6050 \cdot 10^{-3}$	**4.3**	$4.1663 \cdot 10^{-4}$	**3.9**
	$1.2811 \cdot 10^{-1}$	$4.3449 \cdot 10^{-4}7$	**5.4**	$1.0065 \cdot 10^{-4}$	**5.8**
WENO-AO(5,3) ALE (moving mesh)	$3.2742 \cdot 10^{-1}$	$2.6027 \cdot 10^{-2}$	–	$9.2958 \cdot 10^{-3}$	**-**
	$2.5095 \cdot 10^{-1}$	$5.2638 \cdot 10^{-3}$	**6.0**	$1.3474 \cdot 10^{-3}$	**7.3**
	$1.6754 \cdot 10^{-1}$	$8.5469 \cdot 10^{-4}$	**4.5**	$2.2682 \cdot 10^{-4}$	**4.1**
	$1.2778 \cdot 10^{-1}$	$2.2302 \cdot 10^{-4}$	**5.0**	$6.7040 \cdot 10^{-5}$	**5.0**

$$\delta T = -\frac{(\gamma-1)\varepsilon^2}{8\gamma\pi^2} e^{(1-r^2)}; \qquad \delta S = 0$$

where $r^2 = x^2 + y^2$ and the vortex strength $\varepsilon = 5$. The problem is stopped at a time of 10.0, by which time the vortex has propagated a distance of 10 units in the x-direction.

The third order WENO scheme is based on the method described in Section 2. The WENO-AO(4,3) scheme is based on the algorithm described in Section 3.1. The WENO-AO(5,3) scheme is based on the algorithm described in Section 3.2. Table 5 shows that the third order WENO and the WENO-AO(4,3) and WENO-AO(5,3) schemes on fixed and moving meshes achieve their design accuracies. This demonstrates that the WENO-AO reconstruction philosophy presented in this paper works. CFLs as large as 0.5 produce the same order of accuracy on our unstructured mesh.

7. Results – multidimensional test problems

In Section 6 we described the two different types of codes that were used to demonstrate the order of accuracy of the WENO-AO algorithm. In this Section we use the same two codes on a test suite of stringent test problems. For each sub-section we identify the kind of mesh used for that test problem.

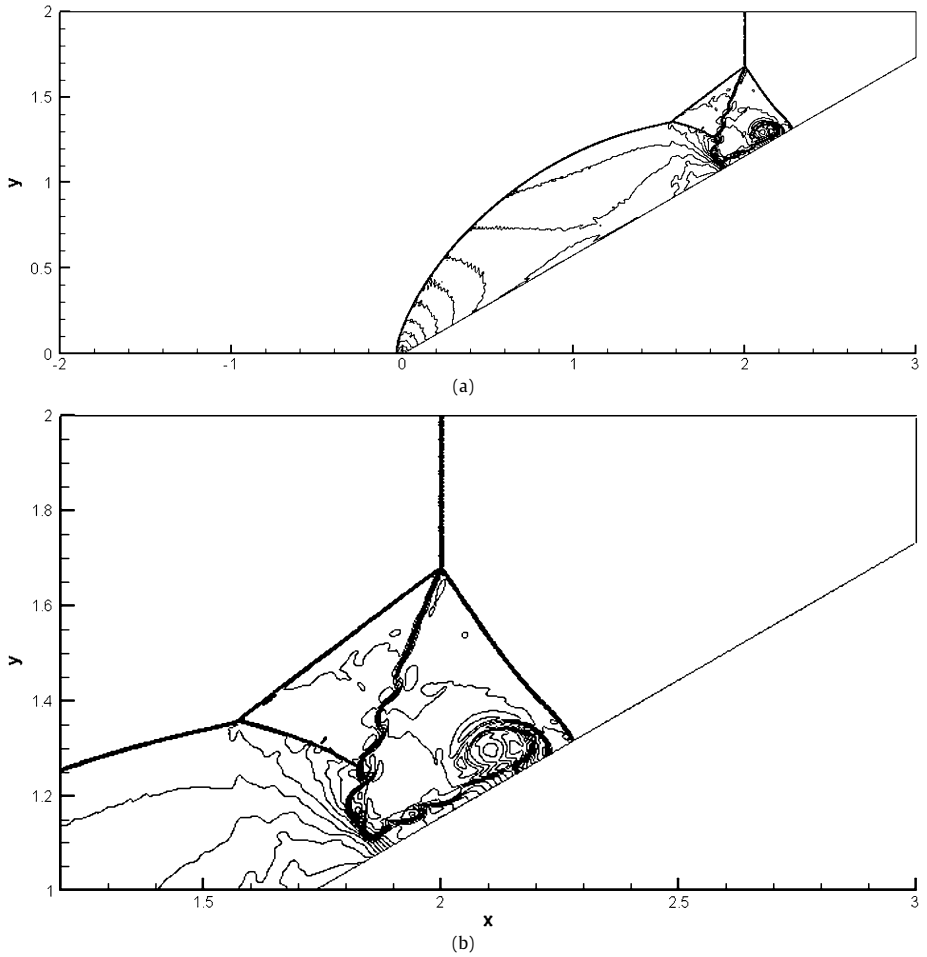

Fig. 4. Plot (a) shows the density at time 0.2 from the double Mach reflection problem run with the fifth order version of the WENO-AO schemes. Plot (b) shows a zoom on the roll-up of the Mach stem in the double Mach reflection problem. Density contour lines are plotted.

7.1. Unstructured static mesh: double Mach reflection problem

This test case has been originally proposed by Woodward and Colella [69] and it involves a Mach 10 shock wave which is moving along the x-direction of the computational domain, where a ramp with an angle of 30° is located. The interaction between the shock wave and the ramp yields the development of small-scale structures that arise from Kelvin-Helmholtz instabilities. The computational domain is discretized with an unstructured mesh of characteristic size $h = 1/400$, hence using 2,690,720 triangles, while the initial condition can be found in the aforementioned reference. The simulation is run to a final time of 0.2 with the fifth order accurate WENO-AO scheme and the results are depicted in Figs. 4a and 4b. Figs. 4a and 4b used 35 density contour levels ranging in the interval [1.5, 22.5]. The high order scheme is able to capture the fluid sub-structures as notable from Fig. 4b, while being at the same time very robust around the strong shock wave.

7.2. Unstructured static mesh: forward facing step problem

The forward facing step problem represents a benchmark for the validation of a numerical scheme in the presence of reflecting shock waves that travel across the computational domain and interact one with each other. The initial condition can be found in the paper by Woodward and Colella [69] and it consists in a Mach 3 flow impinging on a forward facing step. This leads to the generation of a bow shock wave which spreads towards the upper wall boundary of the computational domain. As a result, a normal shock and a slip surface are emanated by the reflecting wall and the interaction among all waves yields a triple point structure in the flow. This test case is run again using the fifth order version of our WENO-AO scheme and Fig. 5 depicts the density contour lines at the final time of 5. A computational mesh with size $h = 1/400$ with 910,992 triangular control volumes has been employed. Figs. 5 used 30 density contour levels ranging in the interval [0.5, 6.5]. High resolution can be noticed at the corner of the forward facing step as well as close to the upper boundary where flow instabilities with vorticial shape occur.

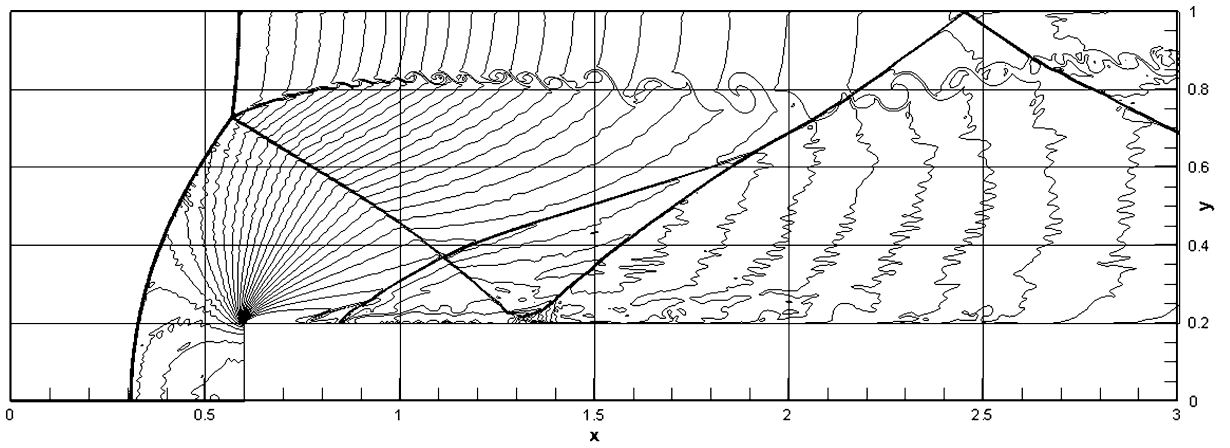

Fig. 5. Shows the density at time 4.0 from the forward facing step problem run with the fifth order version of the WENO-AO schemes.

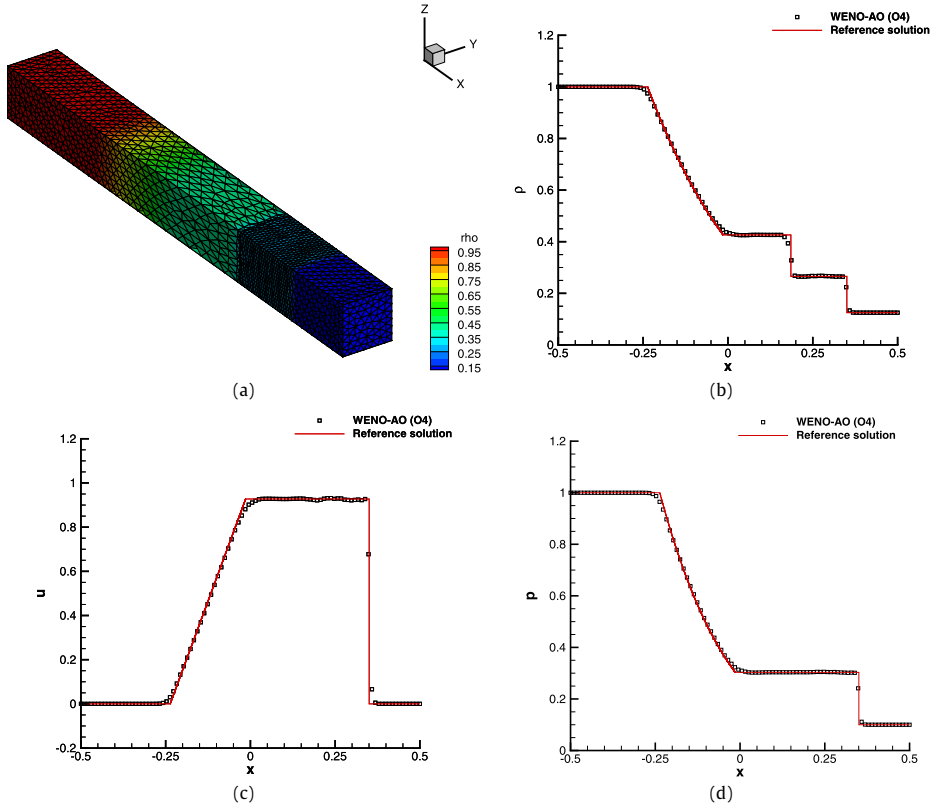

Fig. 6. Shows the results for the Sod problem at time 0.2. (*a*) 3D view of the grid and density contours. Density (*b*), velocity (*c*) and pressure (*d*) versus exact solution.

7.3. Unstructured mesh with ALE: Sod problem on a moving three-dimensional mesh

Here we solve the well-known Sod shock tube problem on a moving unstructured three-dimensional grid. Even though this test case has a one-dimensional setting, it becomes fully multidimensional when run on an unstructured computational mesh where no faces or edges are in general aligned with the main flow along the x-direction. The Sod problem develops a right traveling shock wave and a contact discontinuity, whereas a rarefaction wave is moving to the left. The computational domain is the box $[-0.5, 0.5] \times [-0.05, 0.05] \times [-0.05, 0.05]$ and is discretized with a total number of 22227 tetrahedra. The fourth order WENO-AO scheme has been run to simulate this test case up to the final time 0.2 and the results are gathered in Fig. 6, where a comparison against the exact solution is shown. The numerical results are in excellent agreement and, thanks to the Lagrangian-like approach, only one computational point is located across the contact discontinuity. The mesh

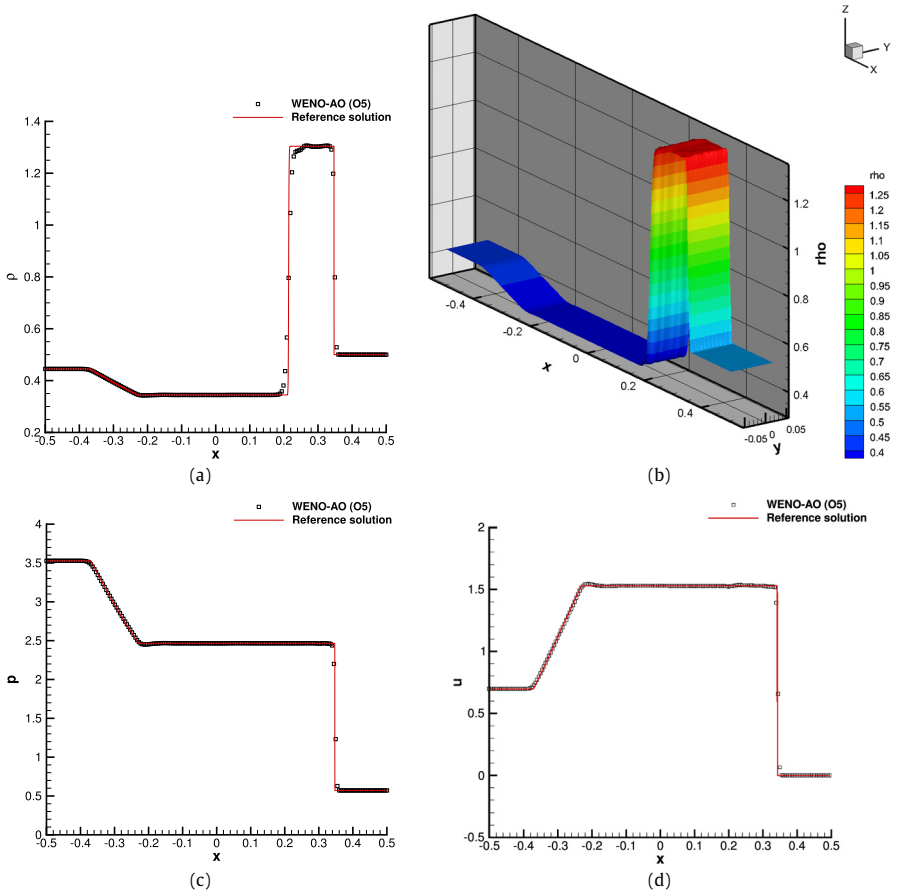

Fig. 7. Shows the results for the Lax problem. Figs. 7a and 7b show two different views of the density, the latter figure shows the density on a 2D unstructured static mesh. Figs. 7c and 7d show the pressure and x-velocity respectively.

is highly compressed by the shock wave and pulled by the rarefaction wave, therefore demonstrating the robustness of the WENO-AO reconstruction proposed in this paper. It is important to appreciate that these are ALE results, and therefore, completely competitive with comparable ALE results from Vilar et al. [68], Liu et al. [55], Chiraville et al. [29], Liu et al. [52] and Loubere et al. [56]. In some cases, our results are even less oscillatory than the ones reported in the literature.

7.4. Unstructured static mesh: Lax problem

Here we solve a classical Riemann problem, namely the Lax shock tube problem. This test case includes the formation of a left-propagating rarefaction wave, an intermediate contact discontinuity and a right-propagating shock wave. Though intrinsically one-dimensional, this problem becomes non-trivial and multidimensional when applied to unstructured meshes, where in general the element edges are not aligned with the fluid motion.

The initial computational domain is given by the box $\Omega = [-0.5; 0.5] \times [-0.05; 0.05]$ that is discretized with a characteristic mesh size of $h = 1/200$, leading to a total number of Ne=8862 elements. The initial conditions are very well-known for the Lax problem and are not repeated here. We fix periodic boundary conditions in the y direction, while transmissive boundaries are imposed along the x direction. The ratio of specific heats is assumed to be $\gamma = 1.4$ and the exact solution is computed with the exact Riemann solver. The final time is $t_f = 0.14$ and we use a fifth order WENO-AO schemes to compute the numerical solution depicted in Fig. 7. A good agreement with the analytical solution can be observed and the scheme is able to preserve the one-dimensional property even at high order and on a two-dimensional unstructured mesh.

7.5. Unstructured mesh with ALE: Saltzman problem

The Saltzman problem consists in the motion of a piston traveling along the main direction of a rectangular box, which is initially filled with a perfect gas at rest with very low pressure. This test problem was set up (Dukovicz and Meltz [76]) for a two-dimensional Cartesian grid that has been skewed and it represents a very challenging test problem that allows the robustness of any moving mesh scheme to be validated. The piston generates a shock wave that is moving faster and is compressing the fluid and, as such, even the computational grid. The final time is 0.6 and a scatter plot of

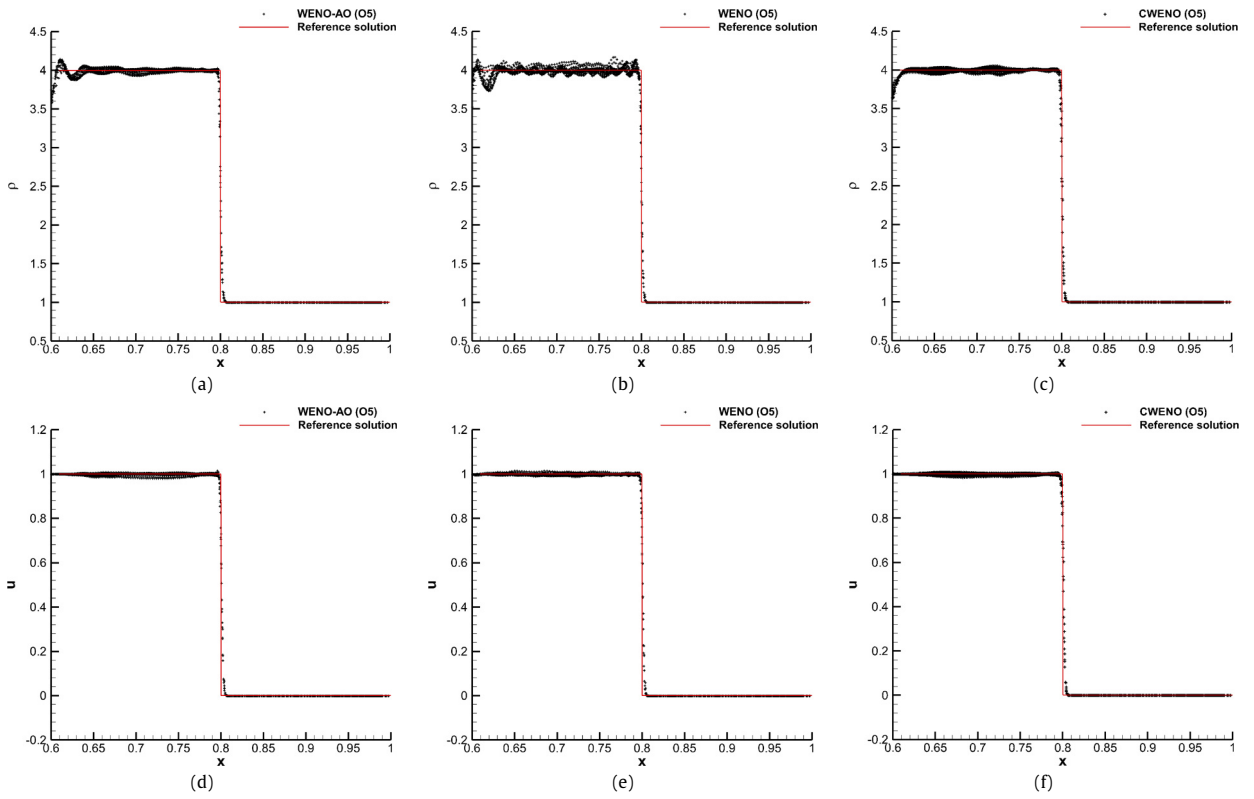

Fig. 8. (a) and (b) show scatter plots of cell density for the Saltzman problem run with the fifth order accurate WENO-AO scheme (left) and the classical fifth order WENO reconstruction (right). Fig. 8c shows the same result computed with CWENO5. Figs. 8d and 8e show scatter plots of cell velocity for the Saltzman problem run with the fifth order accurate WENO-AO scheme (left) and the classical fifth order WENO reconstruction (right). Fig. 8f shows the same result computed with CWENO5.

all cell density and velocity is compared against the exact solution in Figs. 8a, b, c and 8d, e, f, respectively. The numerical results have been obtained with a fifth order WENO-AO scheme on a computational grid with characteristic mesh size of $h = 1/100$, as usually done in literature. For comparison purposes, we have added Figs. 8c and 8f to the aforementioned figures, which show the density and horizontal velocity distribution for the Saltzman problem computed with the CWENO5 algorithm of [36]. The numerical solution is in good agreement with the exact solution and the WENO-AO reconstruction is able to provide a less oscillatory solution compared with standard WENO reconstruction of the same order of accuracy. Our ALE results are competitive with comparable ALE results from Vilar et al. [68], Liu et al. [55], Chiraville et al. [29], Liu et al. [52] and Loubere et al. [56]. In some cases, our results are even less oscillatory than the ones reported in the literature.

7.6. Unstructured mesh with ALE: Sedov problem

We consider both the two- and three-dimensional version of the Sedov problem, that describes the evolution of a cylindrical and spherical symmetric blast wave generated at the origin of the square and cubic computational domain. The origin is located at $\mathbf{O} = (0, 0, 0)$ and the size of the domain is given by $[0, 1.2]^d$ with $d = 2, 3$ being the number of space dimensions. The computational grid is made by triangles or tetrahedra with a mesh size of $h = 0.03$ and the initial set up of this problem can be found in (Boscheri [26]). We use a fifth order WENO-AO scheme in 2D while we rely on the fourth order version in 3D to run the simulation up to time 1.0. The exact solution consists in the shock wave located at radius $r = 1$ with a density peak of 6. Fig. 9 contains the final mesh configurations obtained by the numerical solution, while in Fig. 10 a scatter plot of the cell density is compared with the exact solution for both 2D and 3D configurations. The shock is properly captured and located by the WENO-AO schemes and also the density peak value is well approximated. Note also that the solution is reasonably symmetric and not spread, which is not trivial in the case of high order methods on fully unstructured meshes. Our ALE results are competitive with comparable ALE results from Vilar et al. [68], Liu et al. [55], Chiraville et al. [29], Liu et al. [52] and Loubere et al. [56]. In some cases, our results are even less oscillatory than the ones reported in the literature.

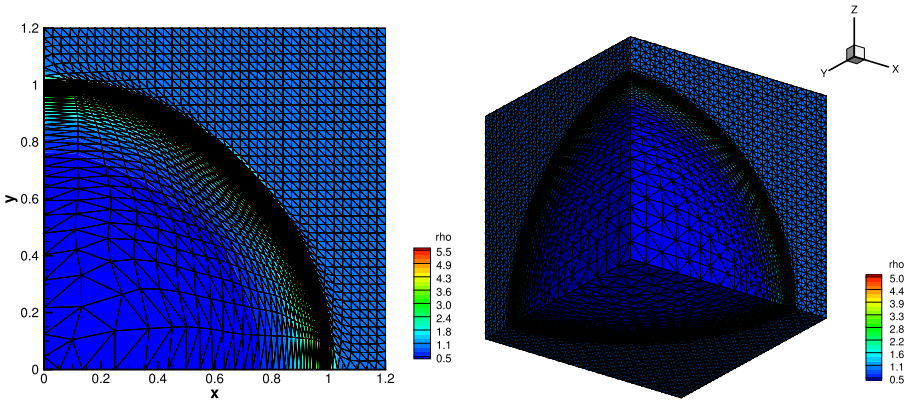

(a) (b)

Fig. 9. Shows the final mesh configuration at time 1.0 for the Sedov problem in 2D (a) and 3D (b).

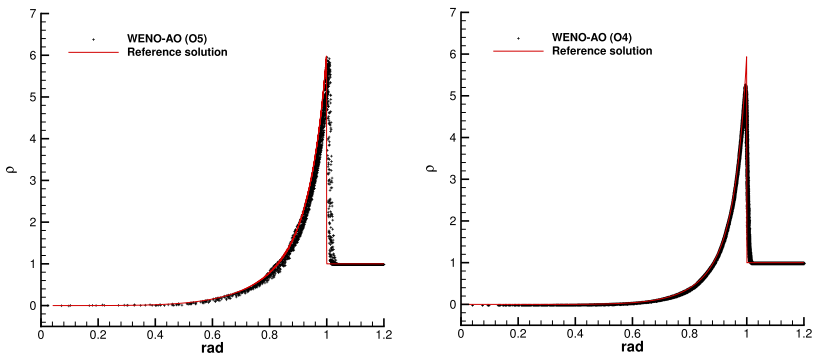

(a) (b)

Fig. 10. Shows a scatter plot of cell density for the Sedov problem in 2D (a) and 3D (b) run with the fifth and fourth order accurate WENO-AO scheme.

7.7. Unstructured mesh with ALE: on the computational efficiency

In the following we want briefly to give some comments on the computational cost of the WENO-AO schemes presented in this paper compared with the WENO schemes proposed in Dumbser and Käser [34] and (Boscheri [26]). In the present work only five (in 2D) or six (in 3D) reconstruction stencils are needed to carry out the reconstruction procedure, while in Dumbser and Käser [34] we always need seven and nine reconstruction stencils in two and three space dimensions, respectively. Moreover, the WENO-AO strategy makes use of a more compact stencil, whose extension is basically determined by the higher polynomial, i.e. the so-called large central stencil. Then, the remaining third order central and one-sided stencils are likely to be contained in the fourth or fifth order central reconstruction stencil. On the contrary, in the WENO approach all stencils are always filled up with the same number of elements dictated by the degree of the reconstruction polynomial, that is 3 or 4 according to what considered in this paper. In this way, the local reconstruction system that has to be solved for each element is bigger in WENO algorithms and each cell counts more reconstruction systems that must be solved, namely one per stencil. The WENO-AO technique allows the reconstruction algorithm to be performed more efficiently but always keeping the desired order of accuracy achieved by classical WENO schemes.

In Table 6 we have collected some information about the computational cost needed for performing the simulation of the Sedov, the Saltzman and the Sod problems in 2D. The first two problems were done on a moving mesh and the Sod problem was done on a fixed two-dimensional mesh. For the first two test cases the mesh is moving, hence requiring the reconstruction matrixes to be computed at each time step. The overall CPU time is provided together with the computational times τ^{W}, τ^{CW} and $\tau^{\mathrm{W\text{-}AO}}$ that account for the time used per element update. Finally, the ratio $\beta = (\tau^{\mathrm{W}}/\tau^{\mathrm{W\text{-}AO}})$ states that the new WENO-AO approach is up to 1.8 times faster than the original WENO algorithm of Boscheri [26]. For CWENO from [36] the WENO-AO is slightly slower because CWENO uses smaller, piecewise linear stencils for its lower order scheme. Thus the speed comparison between WENO-AO and CWENO for ALE approaches actually reflects, to some measure, the stencil selection process. For Eulerian simulations on fixed meshes the gain in time is not as much relevant as for ALE computations because all reconstruction matrixes can be precomputed and stored once and for all in the preprocessing stage. Nevertheless, the WENO-AO strategy requires much less memory thanks to the reduced number of reconstruction stencils and their compactness compared to the original WENO. This is reflected in the results for the Sod problem.

Table 6
Shows the computational time for running the two-dimensional Sedov and Saltzman problems using both WENO-AO and WENO and CWENO methods.

Test	Scheme	# cells	CPU time	# time steps	τ	β
Sedov 2D	WENO – AO	3200	$3.57 \cdot 10^3$	635	$\tau^{\text{W-AO}}$=$1.76 \cdot 10^{-3}$	**1.0**
Sedov 2D	WENO	3200	$8.88 \cdot 10^3$	857	$\tau^{\text{W}} = 3.24 \cdot 10^{-3}$	**1.8**
Sedov 2D	CWENO	3200	$3.54 \cdot 10^3$	752	τ^{CW}=$1.46 \cdot 10^{-3}$	**0.8**
Saltzman 2D	WENO – AO	2000	$3.99 \cdot 10^3$	1074	$\tau^{\text{W-AO}}$=$1.86 \cdot 10^{-3}$	**1.0**
Saltzman 2D	WENO	2000	$1.09 \cdot 10^4$	1823	$\tau^{\text{W}} = 2.98 \cdot 10^{-3}$	**1.6**
Saltzman 2D	CWENO	2000	$3.11 \cdot 10^3$	1053	τ^{CW}=$1.48 \cdot 10^{-3}$	**0.8**
RP2D	WENO – AO	2246	$4.46 \cdot 10^3$	215	$\tau^{\text{W-AO}}$=$9.24 \cdot 10^{-3}$	**1.0**
RP2D	WENO	2246	$4.47 \cdot 10^3$	215	$\tau^{\text{W}} = 9.25 \cdot 10^{-3}$	**1.0**
RP2D	CWENO	2246	$4.45 \cdot 10^3$	215	τ^{CW}=$9.15 \cdot 10^{-3}$	**1.0**

7.8. Spherical geodesic mesh: Sod test

Here we present the results of the well-known Sod shock tube problem. We set up the problem on a spherical computational domain with radial extent $[0.5 : 1.5]$. The diaphragm separating the two uniform states is placed at $r = 1.0$. The vector of primitive variables inside and outside of the diaphragm are given by

$$\begin{pmatrix} \rho \\ \vec{V} \\ P \end{pmatrix}_{in} = \begin{pmatrix} 1 \\ 0 \\ 1 \end{pmatrix}; \qquad \begin{pmatrix} \rho \\ \vec{V} \\ P \end{pmatrix}_{out} = \begin{pmatrix} 0.125 \\ 0 \\ 0.1 \end{pmatrix}$$

We use outflow boundary condition on both the inner and outer radial boundaries.

We run the above set up on the spherical mesh having angular resolution of 5.625° and 256 logarithmically binned radial zones. The computation uses fourth order accurate WENO-AO reconstruction. We also use third order isoparametric mapping to map triangular prisms to the spherical frustrums. The simulation has been run till a time of 0.2. The results of the Sod shock problem on a geodesic mesh are shown in Fig. 11. Fig. 11a shows the mesh, as projected on to the unit sphere. The three solid blue dots in Fig. 11a show us the vertices of one of the great triangles on the sphere. The blue lines also enable us to identify one of the great triangles. We can now easily visualize how recursive subdivision can produce the spherical mesh shown in Fig. 11a. Fig. 11b shows a meridional slice of the spherical mesh with the colorized density; we see that the density is entirely isotropic. Figs. 11c, 11d and 11e show the density, pressure and radial velocity from this spherical Sod shock problem plotted with respect to the radius of the mesh. We see that the contact discontinuity is captured very crisply and the shocks are free of oscillations.

7.9. Spherical geodesic mesh: hydrodynamical blast on a spherical sector

Here we present the results of the three dimensional hydrodynamical blast problem simulated on a spherical sector with radial extent $[7, 16]$. Around radius 11.5, a spherical explosion zone of unit radius is set up with a high pressure of 100 and density of 1. Outside this explosion zone, the pressure is 1 and density is 1. The fluid is initially static.

The above set up is run on a single sector spherical geodesic mesh with angular resolution of 0.35° and 180 logarithmically binned radial zones. Along the triangular edges of the sector we had 128 zones in each direction. We used the third order accurate WENO-AO for the results shown here. Fig. 12 shows the results of the blast problem at a time of 0.2. Fig. 12a and 12b show the density in two different slice planes that pass through the original center of the blast. Fig. 12c and 12d show the pressure in the same two slice planes. Fig. 12e and 12f show the magnitude of the velocity in the same two slice planes. We can detect a slight anisotropy in the density and velocity owing to the fact that we have a ratioed mesh, but the mesh-imprinting is slight.

7.10. Unstructured static mesh: two interacting blast waves

This test problem (Woodward and Colella [69], Jiang and Shu [47]) involves the interaction of two blast waves. Let us consider a two-dimensional unstructured mesh that covers the computational domain $\Omega = [0, 1] \times [0, 0.1]$ and the initial condition specified by the vector of primitive variables given by

$$V(t = 0) = \begin{cases} (1, 0, 0, 1000) & \text{for } 0 < x < 0.1 \\ (1, 0, 0, 0.01) & \text{for } 0.1 < x < 0.9 \\ (1, 0, 0, 100) & \text{for } 0.9 < x < 1 \end{cases}$$

with the adiabatic index $\gamma = 1.4$. The vector of primitive variables in this problem consists of density, x-velocity, y-velocity and pressure. Reflective wall boundary conditions are imposed along the x-direction, while periodic boundaries have been used in y-direction. Two runs were carried out with different resolutions. The computational domain in those two runs was

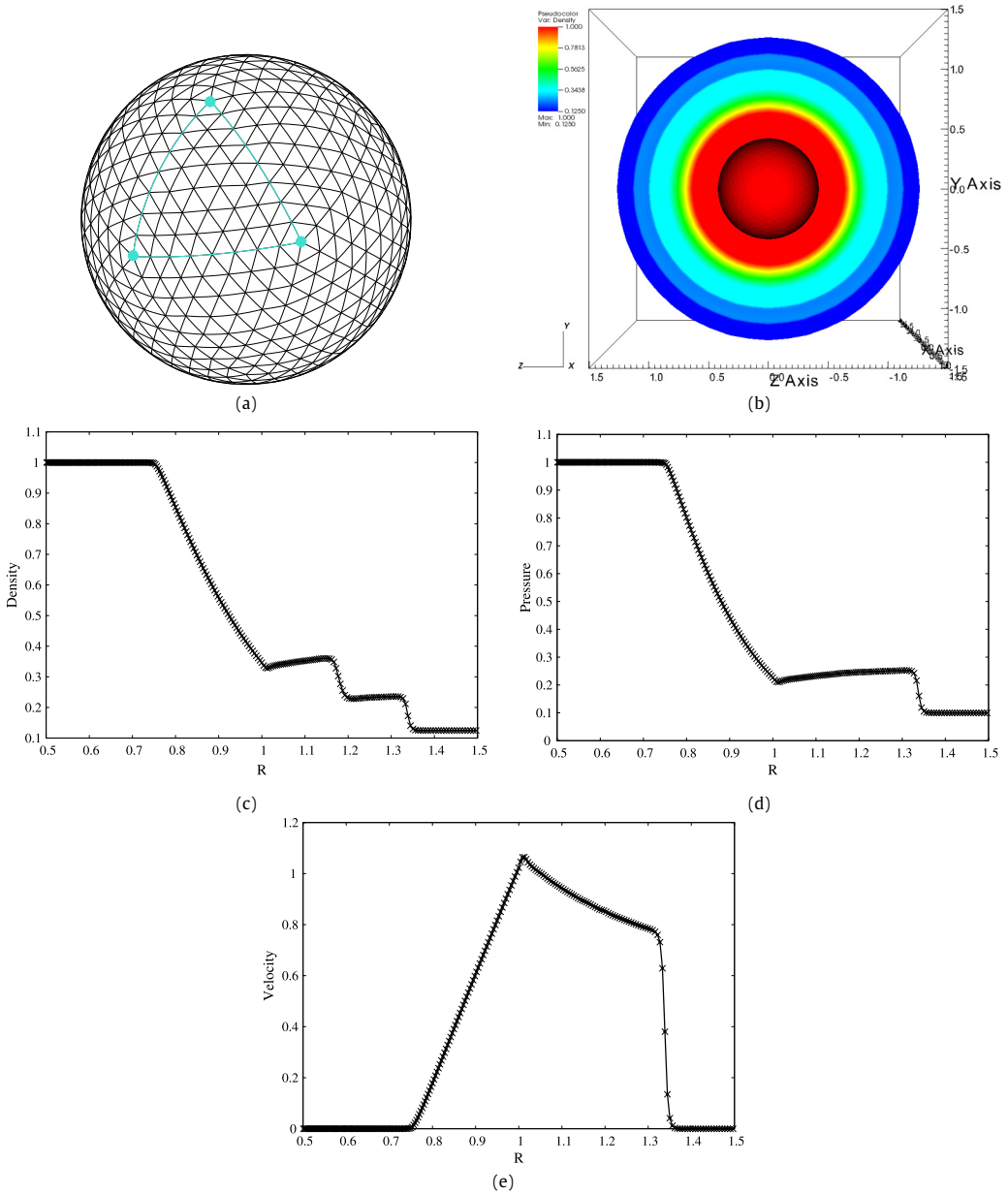

Fig. 11. The results of the Sod shock problem on a geodesic mesh are shown in Fig. 11. Fig. 11a shows the mesh, as projected on to the unit sphere. Fig. 11b shows a meridional slice of the spherical mesh with the colorized density; we see that the density is entirely isotropic. Figs. 11c, 11d and 11e show the density, pressure and radial velocity plotted with respect to the radius of the mesh.

covered with triangular control volumes of two different sizes, namely $h_1 = 1/400$ and $h_2 = 1/600$. The final time of the simulation is chosen to be $t = 0.038$ and the results for both density and pressure distribution for a WENO-AO fifth order scheme are shown in Fig. 13. An excellent agreement with the reference solution is achieved, especially for the computation run on the finer mesh. We underline the fact that this simulation has been actually carried out on a fully two-dimensional unstructured mesh, thus the computational grid is not aligned with the main flow and does not exhibit a one-dimensional property. Nevertheless, the numerical solution presents a very good symmetry w.r.t. the y-axis, since the scatter plots in Fig. 13 refer to *all* cell values (i.e., it is not a 1D cut across the 2D domain).

7.11. Unstructured static mesh: shock density interaction problem

In order to show the advantages of high order numerical scheme, we propose to solve a well-known test problem (Shu and Osher [60,61]) that considers the interaction of a shock wave at Mach number $M = 3$ with a density fluctuation. Specifically, the computational domain is given by $\Omega = [-5, 5] \times [-0.075, 0.075]$ and is discretized with an unstructured

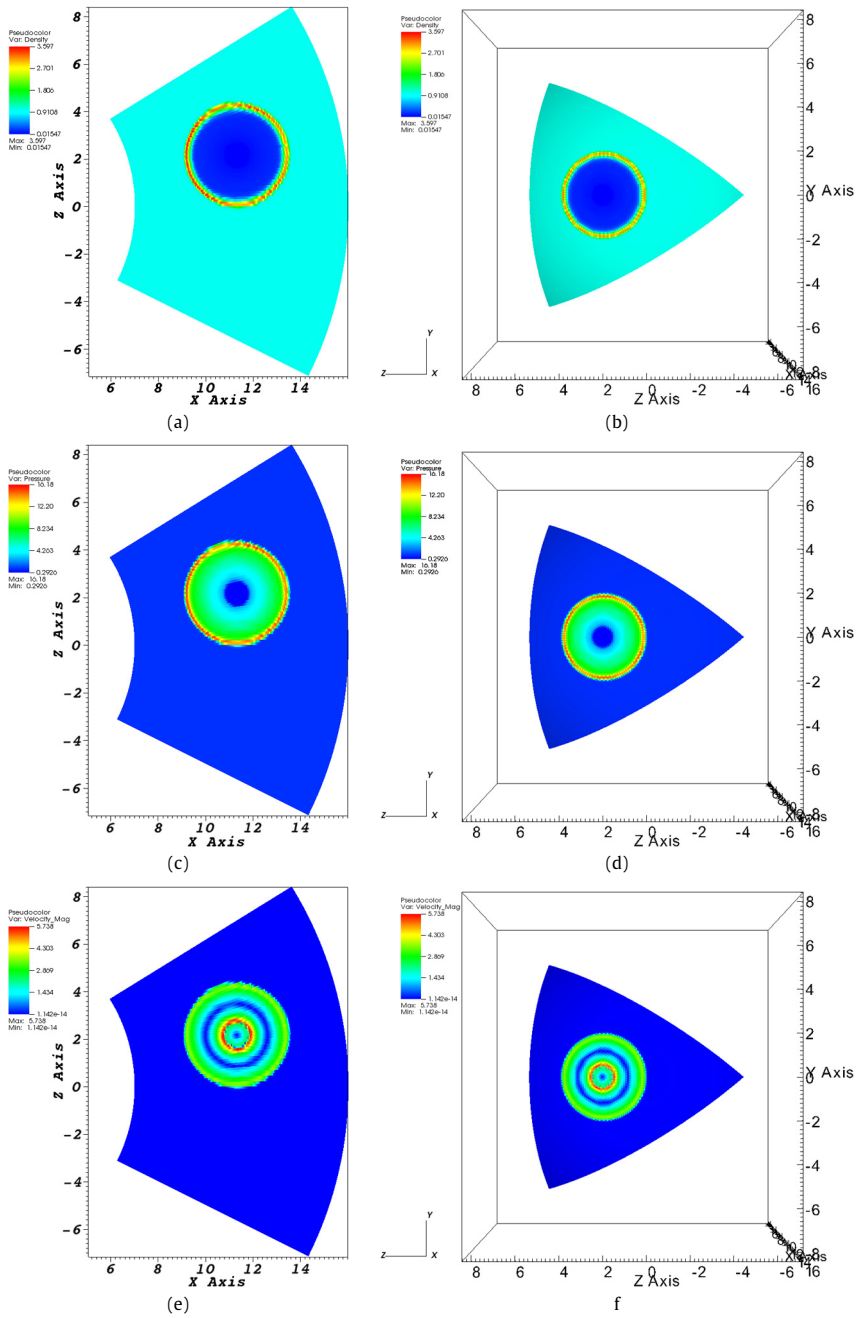

Fig. 12. Shows the results of the blast problem at a time of 0.2. Fig. 12a and 12b show the density in two different slice planes that pass through the original center of the blast. Fig. 12c and 12d show the pressure in the same two slice planes. Fig. 12e and 12f show the magnitude of the velocity in the same two slice planes.

triangular grid of characteristic mesh size $h = 0.025$. Since we use an unstructured mesh, in general the element edges are not aligned with the coordinate axes. The total number of control volumes reads NE $= 5560$, corresponding to an equivalent one-dimensional resolution of 1/400 cells along the x-direction. The initial conditions are exactly the ones specified in the original reference cited above. The ratio of specific heats of the gas is $\gamma = 1.4$ and the final time of the simulation is set to $t = 1.8$. Dirichlet and periodic boundary conditions are imposed in x- and y-direction, respectively. Figs. 14a and 14b depict the numerical density distribution for both fourth and fifth order WENO-AO schemes. A zoom on the density oscillations is also shown in Fig. 14c. The fifth order scheme better resolves the flow feature and an overall good agreement with the reference solution can be observed.

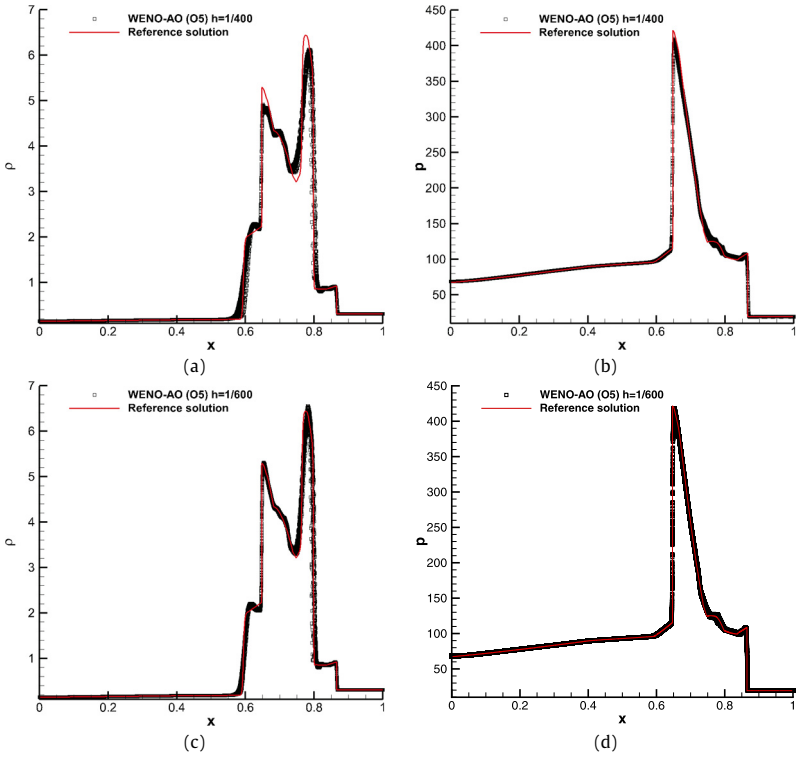

Fig. 13. Shows the density and pressure of the two interacting blast waves problem run with the WENO-AO algorithm on two-dimensional unstructured meshes with zone sizes of 1/400 and 1/600. Figs. 13a and 13b show density and pressure for the lower resolution simulation. Figs. 13c and 13d show density and pressure for the higher resolution simulation. The reference solution is also shown.

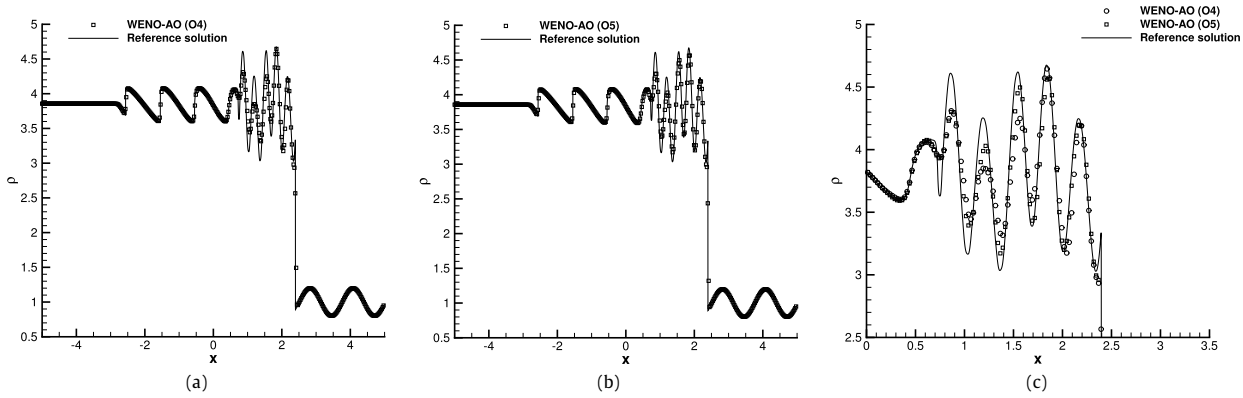

Fig. 14. 14a and 14b depict the numerical density distribution for both fourth and fifth order WENO-AO schemes for the shock-density interaction problem. A zoom on the density oscillations is also shown in Fig. 14c.

8. Conclusions

In Balsara, Garain and Shu [14] a WENO-AO method was developed for finite difference WENO schemes on structured meshes. However, real-world problems are simulated on unstructured meshes. These meshes can be adapted to treat the geometric complexity that is inherent in real-world problems. The meshes can also themselves adapt to the solution, as in the case of an ALE scheme. For all such situations, it is highly desirable to reformulate the WENO-AO reconstruction method to arbitrary meshes. In this paper we have accomplished such a goal. The WENO-AO(4,3) and WENO-AO(5,3) schemes presented here can provide very high order of accuracy for smooth flow while also reverting to a very stable third order scheme that has excellent shock-handling capabilities as well as the ability to preserve extrema.

The method presented in this paper derives its efficiency from a fundamental insight that is taught in freshman physics classes. This insight consists of realizing that the moment of inertia of a solid about an axis that passes through its center of mass can be related to the moment of inertia of the same solid about any other axis that is parallel to the original axis. (In

classical mechanics, this is known as the Parallel Axis Theorem or the Huygens-Steiner Theorem.) This fundamental insight from freshman physics is generalized very significantly in this paper to arrive at a particularly convenient Taylor basis set in which the reconstructed variables can be expanded. The basis is very useful when reconstructing the solution on a given target zone. This is because the basis set in the target zone can be related to the basis set in another zone that is part of the target zone's stencil. This is done via a simple transformation that generalizes the Parallel Axis Theorem. This generalization dramatically simplifies the reconstruction procedure on any given stencil. A consequence of this simplification is that instead of solving a constrained least squares problem (Dumbser and Kaser [34], Dumbser et al. [36]), one has only to solve a much simpler least squares problem. This convenient basis set is also beneficial when constructing smoothness indicators.

As with finite-difference WENO, we realize that one can make a non-linear hybridization between a large, centered, very high accuracy stencil and a lower order central WENO scheme that is, nevertheless, very stable and capable of capturing physically meaningful extrema. The result is a class of adaptive order WENO schemes that work very well on unstructured meshes. The smaller stencils (that are non-linearly hybridized with a larger, high order stencil) consist of the set of CWENO-type stencils that are traditionally used for third order WENO calculations on unstructured meshes.

Via a sequence of accuracy tests on a range of different mesh types, we show that the method meets its design accuracy. Several stringent test problems are presented to demonstrate that the method works very robustly and very well. The test problems are chosen to show that our method can be applied to many different types of unstructured meshes that are used to map geometric complexity or solution complexity. Our test problems encompass geodesic meshes, unstructured meshes and ALE-type meshes. Our WENO-AO method is also shown to be more efficient compared to older WENO schemes for unstructured meshes.

Declaration of competing interest

The authors declare that they have no known competing financial interests or personal relationships that could have appeared to influence the work reported in this paper.

Acknowledgements

DSB acknowledges support via NSF grants NSF-ACI-1533850, NSF-DMS-1622457, NSF-ACI-1713765, NSF-DMS-1821242 and NSF-ECCS-19-04774. VAF acknowledges support via NSF grants NSF-DMS-1361197. Several simulations were performed on a cluster at UND that is run by the Center for Research Computing. Computer support on NSF's XSEDE and Blue Waters computing resources is also acknowledged.

Appendix A

In the text, eqn. (2.12), (2.13) and (2.14) as well as (3.5), (3.6), (3.7) and (3.8) have given all the expressions for implementing WENO-AO for two dimensions. Those expressions go over unchanged to three dimensions. In this appendix, we provide all the supplemental expressions for implementing WENO-AO in three dimensions up to fourth order. Once this idea is understood, extensions to fifth order are also easy.

In three dimensions, we have (x, y, z) coordinates with a shift given by (ξ, η, ζ). Therefore, we can write the supplemental expressions for the third order WENO-AO as

$$\iiint_{\Delta_j} \left[(\zeta + z_j)^2 - \bar{C}^0_{zz}\right] d\xi\, d\eta\, d\zeta = |\Delta_j| l_0^2 \left\{ \left[\left(\frac{z_j}{l_0}\right)^2 - C^0_{zz} \right] + \left(\frac{l_j}{l_0}\right)^2 C^j_{zz} \right\} \tag{A.1}$$

$$\iiint_{\Delta_j} \left[(\xi + x_j)(\zeta + z_j) - \bar{C}^0_{xz}\right] d\xi\, d\eta\, d\zeta = |\Delta_j| l_0^2 \left\{ \left[\left(\frac{x_j}{l_0}\right)\left(\frac{z_j}{l_0}\right) - C^0_{xz} \right] + \left(\frac{l_j}{l_0}\right)^2 C^j_{xz} \right\} \tag{A.2}$$

$$\iiint_{\Delta_j} \left[(\eta + y_j)(\zeta + z_j) - \bar{C}^0_{yz}\right] d\xi\, d\eta\, d\zeta = |\Delta_j| l_0^2 \left\{ \left[\left(\frac{y_j}{l_0}\right)\left(\frac{z_j}{l_0}\right) - C^0_{yz} \right] + \left(\frac{l_j}{l_0}\right)^2 C^j_{yz} \right\} \tag{A.3}$$

The supplemental expressions for the four order WENO-AO can be written as

$$\iiint_{\Delta_j} \left[(\zeta + z_j)^3 - \bar{C}^0_{zzz}\right] d\xi\, d\eta\, d\zeta = |\Delta_j| l_0^3 \left\{ \left[\left(\frac{z_j}{l_0}\right)^3 - C^0_{zzz} \right] + 3\left(\frac{z_j}{l_0}\right)\left(\frac{l_j}{l_0}\right)^2 C^j_{zz} + \left(\frac{l_j}{l_0}\right)^3 C^j_{zzz} \right\} \tag{A.4}$$

$$\begin{aligned} &\iiint_{\Delta_j} \left[(\xi + x_j)^2(\zeta + z_j) - \bar{C}^0_{xxz}\right] d\xi\, d\eta\, d\zeta \\ &= |\Delta_j| l_0^3 \left\{ \left[\left(\frac{x_j}{l_0}\right)^2\left(\frac{z_j}{l_0}\right) - C^0_{xxz} \right] + \left(\frac{z_j}{l_0}\right)\left(\frac{l_j}{l_0}\right)^2 C^j_{xx} + 2\left(\frac{x_j}{l_0}\right)\left(\frac{l_j}{l_0}\right)^2 C^j_{xz} + \left(\frac{l_j}{l_0}\right)^3 C^j_{xxz} \right\} \end{aligned} \tag{A.5}$$

$$\iiint_{\Delta_j} [(\eta + y_j)^2(\zeta + z_j) - \bar{C}^0_{yyz}] d\xi\, d\eta\, d\zeta \tag{A.6}$$
$$= |\Delta_j| l_0^3 \left\{ \left[\left(\frac{y_j}{l_0}\right)^2 \left(\frac{z_j}{l_0}\right) - C^0_{yyz} \right] + \left(\frac{z_j}{l_0}\right)\left(\frac{l_j}{l_0}\right)^2 C^j_{yy} + 2\left(\frac{y_j}{l_0}\right)\left(\frac{l_j}{l_0}\right)^2 C^j_{yz} + \left(\frac{l_j}{l_0}\right)^3 C^j_{yyz} \right\}$$

$$\iiint_{\Delta_j} [(\xi + x_j)(\zeta + z_j)^2 - \bar{C}^0_{xzz}] d\xi\, d\eta\, d\zeta \tag{A.7}$$
$$= |\Delta_j| l_0^3 \left\{ \left[\left(\frac{x_j}{l_0}\right)\left(\frac{z_j}{l_0}\right)^2 - C^0_{xzz} \right] + \left(\frac{x_j}{l_0}\right)\left(\frac{l_j}{l_0}\right)^2 C^j_{zz} + 2\left(\frac{z_j}{l_0}\right)\left(\frac{l_j}{l_0}\right)^2 C^j_{xz} + \left(\frac{l_j}{l_0}\right)^3 C^j_{xzz} \right\}$$

$$\iiint_{\Delta_j} [(\eta + y_j)(\zeta + z_j)^2 - \bar{C}^0_{yzz}] d\xi\, d\eta\, d\zeta \tag{A.8}$$
$$= |\Delta_j| l_0^3 \left\{ \left[\left(\frac{y_j}{l_0}\right)\left(\frac{z_j}{l_0}\right)^2 - C^0_{yzz} \right] + \left(\frac{y_j}{l_0}\right)\left(\frac{l_j}{l_0}\right)^2 C^j_{zz} + 2\left(\frac{z_j}{l_0}\right)\left(\frac{l_j}{l_0}\right)^2 C^j_{yz} + \left(\frac{l_j}{l_0}\right)^3 C^j_{yzz} \right\}$$

$$\iiint_{\Delta_j} [(\xi + x_j)(\eta + y_j)(\zeta + z_j) - \bar{C}^0_{xyz}] d\xi\, d\eta\, d\zeta$$
$$= |\Delta_j| l_0^3 \left\{ \left[\left(\frac{x_j}{l_0}\right)\left(\frac{y_j}{l_0}\right)\left(\frac{z_j}{l_0}\right) - C^0_{xyz} \right] + \left(\frac{z_j}{l_0}\right)\left(\frac{l_j}{l_0}\right)^2 C^j_{xy} + \left(\frac{y_j}{l_0}\right)\left(\frac{l_j}{l_0}\right)^2 C^j_{xz} + \left(\frac{x_j}{l_0}\right)\left(\frac{l_j}{l_0}\right)^2 C^j_{yz} + \left(\frac{l_j}{l_0}\right)^3 C^j_{xyz} \right\} \tag{A.9}$$

References

[1] R. Abgrall, On essentially non-oscillatory schemes on unstructured meshes: analysis and implementation, J. Comput. Phys. 144 (1994) 45–58.
[2] T. Aboiyar, E.H. Georgoulis, A. Iske, Adaptive ADER methods using kernel-based polyharmonic spline WENO reconstruction, SIAM J. Sci. Comput. 32 (6) (2010) 3251–3277.
[3] F. Aràndiga, A. Baeza, A.M. Belda, P. Mulet, Analysis of WENO schemes for full and global accuracy, SIAM J. Numer. Anal. 49 (2) (2011) 893–915.
[4] D.S. Balsara, C.-W. Shu, Monotonicity preserving weighted non-oscillatory schemes with increasingly high order of accuracy, J. Comput. Phys. 160 (2000) 405–452.
[5] D.S. Balsara, Divergence-free adaptive mesh refinement for magnetohydrodynamics, J. Comput. Phys. 174 (2) (2001) 614–648.
[6] D.S. Balsara, Second order accurate schemes for magnetohydrodynamics with divergence-free reconstruction, Astrophys. J. Suppl. Ser. 151 (1) (2004) 149–184.
[7] D.S. Balsara, T. Rumpf, M. Dumbser, C.-D. Munz, Efficient, high-accuracy ADER-WENO schemes for hydrodynamics and divergence-free magnetohydrodynamics, J. Comput. Phys. 228 (2009) 2480.
[8] D.S. Balsara, Divergence-free reconstruction of magnetic fields and WENO schemes for magnetohydrodynamics, J. Comput. Phys. 228 (2009) 5040–5056.
[9] D.S. Balsara, Multidimensional extension of the HLLE Riemann solver; application to Euler and magnetohydrodynamical flows, J. Comput. Phys. 229 (2010) 1970–1993.
[10] D.S. Balsara, A two-dimensional HLLC Riemann solver with applications to Euler and MHD flows, J. Comput. Phys. 231 (2012) 7476–7503.
[11] D.S. Balsara, Self-adjusting, positivity preserving high order schemes for hydrodynamics and magnetohydrodynamics, J. Comput. Phys. 231 (2012) 7504–7517.
[12] D.S. Balsara, Multidimensional Riemann problem with self-similar internal structure – Part I – Application to hyperbolic conservation laws on structured meshes, J. Comput. Phys. 277 (2014) 163–200.
[13] D.S. Balsara, M. Dumbser, Divergence-free MHD on unstructured meshes using high order finite volume schemes based on multidimensional Riemann solvers, J. Comput. Phys. 299 (2015) 687–715.
[14] D.S. Balsara, S. Garain, C.-W. Shu, An efficient class of WENO schemes with adaptive order, J. Comput. Phys. 326 (2016) 780–804.
[15] D.S. Balsara, B. Nkonga, Formulating multidimensional Riemann solvers in similarity variables – Part III: A multidimensional analogue of the HLLI Riemann solver for conservative hyperbolic systems, J. Comput. Phys. 346 (2017) 25–48.
[16] D.S. Balsara, T. Amano, S. Garain, J. Kim, High order accuracy divergence-free scheme for the electrodynamics of relativistic plasmas with multidimensional Riemann solvers, J. Comput. Phys. 318 (2016) 169–200.
[17] D.S. Balsara, A. Taflove, S. Garain, G. Montecinos, Computational electrodynamics in material media with constraint-preservation, multidimensional Riemann solvers and sub-cell resolution – Part I, Second-order FVTD schemes, J. Comput. Phys. 349 (2017) 604–635.
[18] D.S. Balsara, A. Taflove, S. Garain, G. Montecinos, Computational electrodynamics in material media with constraint-preservation, multidimensional Riemann solvers and sub-cell resolution – Part II, Higher-order FVTD schemes, J. Comput. Phys. 354 (2018).
[19] D.S. Balsara, Higher order accurate space-time schemes for computational astrophysics – Part I – Finite volume methods, Living Rev. Comput. Astrophys. (2017).
[20] D.S. Balsara, V. Florinski, S. Garain, S. Subramanyan, K.F. Gurski, Efficient, divergence-free high order MHD on 3D spherical meshes with optimal geodesic mapping, Mon. Not. R. Astron. Soc. 487 (2019) 1283.
[21] T. Barth, P. Frederickson, Higher Order Solution of the Euler Equations on Unstructured Grids Using Quadratic Reconstruction, AIAA Paper 90-0013, 1990.
[22] R. Borges, M. Carmona, B. Costa, W.S. Don, An improved weighted essentially non-oscillatory scheme for hyperbolic conservation laws, J. Comput. Phys. 227 (6) (2008) 3101–3211.

[23] W. Boscheri, M. Dumbser, D.S. Balsara, High order Lagrangian ADER-WENO schemes on unstructured meshes – application of several node solvers to hydrodynamics and magnetohydrodynamics, Int. J. Numer. Methods Fluids 76 (10) (2014) 737–778.
[24] W. Boscheri, D.S. Balsara, M. Dumbser, Lagrangian ADER-WENO finite volume schemes on unstructured triangular meshes based on genuinely multidimensional HLL Riemann solvers, J. Comput. Phys. 267 (2014) 112–138.
[25] W. Boscheri, M. Dumbser, A direct arbitrary-Lagrangian-Eulerian ADER-WENO finite volume scheme on unstructured tetrahedral meshes for conservative and non-conservative hyperbolic systems in 3D, J. Comput. Phys. 275 (2014) 484–523.
[26] W. Boscheri, High order direct arbitrary-Lagrangian Eulerian (ALE) finite volume schemes for hyperbolic systems on unstructured meshes, Arch. Comput. Meth. Eng. (2016) 1–51.
[27] W. Boscheri, M. Dumbser, High order accurate direct arbitrary-Lagrangian-Eulerian ADER-WENO finite volume schemes on moving curvilinear unstructured meshes, Comput. Fluids 136 (2016) 48–66.
[28] M. Castro, B. Costa, W.S. Don, High order weighted essentially non-oscillatory WENO-Z schemes for hyperbolic conservation laws, J. Comput. Phys. 230 (2011) 1766–1792.
[29] V.P. Chiravalle, N.R. Morgan, A 3D Lagrangian cell-centered hydrodynamic method with higher-order reconstructions for gas and solid dynamics, J. Comput. Phys. 373 (2018) 253–283.
[30] I. Cravero, M. Semplice, On the accuracy of WENO and CWENO reconstructions of third order on nonuniform meshes, J. Sci. Comput. 67 (3) (1 June 2016) 1219–1246.
[31] I. Cravero, G. Puppo, M. Semplice, G. Visconti, CWENO: uniformly accurate reconstructions for balance laws, Math. Comput. 87 (2018) 1689–1719.
[32] X. Deng, H. Zhang, Developing high order weighted compact nonlinear schemes, J. Comput. Phys. 203 (2005) 22–44.
[33] W.-S. Don, P. Li, K.Y. Wong, Z. Gao, Symmetry-preserving property of high order weighted essentially non-oscillatory finite difference schemes for hyperbolic conservation laws, J. Comput. Phys. (2019), submitted for publication, https://www.researchgate.net/publication/306036129_Improved_Symmetry_Property_of_High_Order_Weighted_Essentially_Non-Oscillatory_Finite_Difference_Schemes_for_Hyperbolic_Conservation_Laws.
[34] M. Dumbser, M. Käser, Arbitrary high order non-oscillatory finite volume schemes on unstructured meshes for linear hyperbolic systems, J. Comput. Phys. 221 (2007) 693–723.
[35] M. Dumbser, D.S. Balsara, E.F. Toro, C.-D. Munz, A unified framework for the construction of quadrature-free one-step finite-volume and discontinuous Galerkin schemes, J. Comput. Phys. 227 (2008) 8209–8253.
[36] M. Dumbser, W. Boscheri, M. Semplice, G. Russo, Central WENO schemes for hyperbolic conservation laws on fixed and moving unstructured meshes, SIAM J. Sci. Comput. 39 (2017) A2564–A2591.
[37] M. Dumbser, R. Saurel, V. Titarev, Recent progress in nonlinear numerical methods for time-dependent flow & transport problems, Comput. Fluids 169 (2018) 71–86.
[38] O. Friedrichs, Weighted essentially non-oscillatory schemes for the interpolation of mean values on unstructured grids, J. Comput. Phys. 144 (1998) 194–212.
[39] G.A. Gerolymos, D. Sénéchal, I. Vallet, Very high order WENO schemes, J. Comput. Phys. 228 (2009) 8481–8524.
[40] H. Goldstein, C.P. Poole, J. Safko, Classical Mechanics, Pearson Education Limited, 2015.
[41] A.E. Haas, Introduction to Theoretical Physics, 1928.
[42] A. Harten, B. Engquist, S. Osher, S. Chakravarthy, Uniformly high order essentially non-oscillatory schemes III, J. Comput. Phys. 71 (1987) 231–303.
[43] A.K. Henrick, T.D. Aslam, J.M. Powers, Mapped weighted essentially non-oscillatory schemes: achieving optimal order near critical points, J. Comput. Phys. 207 (2006) 542–567.
[44] C. Hu, C.-W. Shu, Weighted essentially non-oscillatory schemes on triangular meshes, J. Comput. Phys. 150 (1999) 97–127.
[45] M. Käser, A. Iske, ADER schemes on adaptive triangular meshes for scalar conservation laws, J. Comput. Phys. 205 (2005) 486–508.
[46] X.Y. Hu, Q. Wang, N.A. Adams, An adaptive central-upwind weighted essentially non-oscillatory scheme, J. Comput. Phys. 229 (2010) 8952–8965.
[47] G.-S. Jiang, C.-W. Shu, Efficient implementation of weighted ENO schemes, J. Comput. Phys. 126 (1996) 202–228.
[48] E. Johnsen, et al., Assessment of high-resolution methods for numerical simulations of compressible turbulence with shock waves, J. Comput. Phys. 229 (2010) 1213–1237.
[49] S. Lele, Compact finite difference schemes with spectral-like resolution, J. Comput. Phys. 103 (1992) 16–42.
[50] D. Levy, G. Puppo, G. Russo, Compact central WENO schemes for multidimensional conservation laws, SIAM J. Sci. Comput. 22 (2000) 656–672.
[51] X.-D. Liu, S. Osher, T. Chan, Weighted essentially non-oscillatory schemes, J. Comput. Phys. 115 (1994) 200–212.
[52] W. Liu, J. Cheng, C.-W. Shu, High order conservative Lagrangian schemes with Lax–Wendroff type time discretization for the compressible Euler equations, J. Comput. Phys. 228 (2009) 8872–8891.
[53] H. Luo, J.D. Baum, R. Löhner, A discontinuous Galerkin method based on Taylor basis for the compressible flows on arbitrary grids, J. Comput. Phys. 227 (2008) 8875–8893.
[54] Y. Liu, Y.T. Zhang, A robust reconstruction for unstructured WENO schemes, J. Sci. Comput. 54 (2013) 603–621.
[55] X. Liu, N.R. Morgan, D.E. Burton, Lagrangian discontinuous Galerkin hydrodynamic methods in axisymmetric coordinates, J. Comput. Phys. 373 (2018) 253–283.
[56] R. Loubère, P.H. Maire, M. Shashkov, ReALE: a reconnection arbitrary-Lagrangian–Eulerian method in cylindrical geometry, Comput. Fluids 46 (2011) 59–69.
[57] M.P. Martin, E.M. Taylor, M. Wu, V.G. Weirs, A bandwidth-optimized WENO scheme for the effective direct numerical simulation of compressive turbulence, J. Comput. Phys. 220 (2006) 270–289.
[58] S. Pirozzoli, Conservative hybrid compact-WENO schemes for shock-turbulence interaction, J. Comput. Phys. 178 (2002) 81–117.
[59] M. Semplice, A. Coco, G. Russo, Adaptive mesh refinement for hyperbolic systems based on third-order compact WENO reconstruction, J. Sci. Comput. 66 (2) (1 February 2016) 692–724.
[60] C.-W. Shu, S.J. Osher, Efficient implementation of essentially non-oscillatory shock capturing schemes, J. Comput. Phys. 77 (1988) 439–471.
[61] C.-W. Shu, S.J. Osher, Efficient implementation of essentially non-oscillatory shock capturing schemes II, J. Comput. Phys. 83 (1989) 32–78.
[62] C.-W. Shu, High order weighted essentially non-oscillatory schemes for convection dominated problems, SIAM Rev. 51 (2009) 82–126.
[63] Y.Q. Shen, G.W. Yang, Hybrid finite compact-WENO schemes for shock calculation, Int. J. Numer. Methods Fluids 53 (2007) 531–560.
[64] R.J. Spiteri, S.J. Ruuth, A new class of optimal high-order strong-stability-preserving time-stepping schemes, SIAM J. Numer. Anal. 40 (2002) 469–491.
[65] R.J. Spiteri, S.J. Ruuth, Non-linear evolution using optimal fourth-order strong-stability-preserving Runge-Kutta methods, Int. J. Math. Comput. Simul. 62 (2003) 125–135.
[66] C.K. Tam, J.C. Webb, Dispersion-relation-preserving finite difference schemes for computational acoustics, J. Comput. Phys. 107 (1993) 262–281.
[67] P. Tsoutsanis, V.A. Titarev, D. Drikakis, WENO schemes on arbitrary mixed-element unstructured meshes in three space dimensions, J. Comput. Phys. 230 (2011) 1585.
[68] F. Vilar, P.-H. Maire, R. Abgrall, A discontinuous Galerkin discretization for solving the two-dimensional gas dynamics equations written under total Lagrangian formulation on general unstructured grids, J. Comput. Phys. 276 (2014) 188–234.
[69] P. Woodward, P. Colella, The numerical simulation of two-dimensional fluid flow with strong shocks, J. Comput. Phys. 54 (1984) 115–173.
[70] Z. Xu, D.S. Balsara, H. Du, Divergence-free WENO reconstruction-based finite volume scheme for ideal MHD equations on triangular meshes, Commun. Comput. Phys. 19 (04) (2016) 841–880.

[71] Y.-T. Zhang, C.-W. Shu, Third order WENO scheme on three dimensional tetrahedral meshes, Commun. Comput. Phys. 5 (2009) 836–848.
[72] J. Zhu, J. Qiu, A new fifth order finite difference WENO scheme for solving hyperbolic conservation laws, J. Comput. Phys. 318 (2016) 110–121.
[73] J. Zhu, J. Qiu, A new type of finite volume WENO schemes for hyperbolic conservation laws, J. Sci. Comput. 73 (2017) 1338–1359.
[74] J. Zhu, X. Zhong, C.-W. Shu, J. Qiu, Runge-Kutta discontinuous Galerkin method with a simple and compact Hermite WENO limiter on unstructured meshes, Commun. Comput. Phys. 21 (2017) 623–649.
[75] Z. Zhao, J. Zhu, Y. Chen, J. Qiu, A new hybrid WENO scheme for hyperbolic conservation laws, Comput. Fluids 179 (2019) 422–436.
[76] J.K. Dukovicz, B. Meltz, Vorticity errors in multidimensional Lagrangian codes, J. Comput. Phys. 99 (1992) 115–134.
[77] E.N. Parker, Dynamical theory of the solar wind, Space Sci. Rev. 4 (5–6) (1965) 666–708.
[78] L. Ivan, H. De Sterck, A. Susanto, C.P.T. Groth, High-order central ENO finite-volume scheme for hyperbolic conservation laws on three-dimensional cubed-sphere grids, J. Comput. Phys. 282 (2015) 157–182.
[79] J. Zhu, J. Qiu, New finite volume weighted essentially non-oscillatory schemes on triangular meshes, SIAM J. Sci. Comput. 40 (2) (2018) A903–A928.
[80] S. Zhang, J. Zhu, C.-W. Shu, A brief review on the convergence to steady state solutions of Euler equations with high-order WENO schemes, Adv. Aerodyn. 1 (2019) 1–16.
[81] J. Zhu, J. Qiu, A new third order finite volume weighted essentially non-oscillatory scheme on tetrahedral meshes, J. Comput. Phys. 349 (2017) 220–232.